Chapter 2.

A high-throughput, quantitative cell-based screen for efficient tailoring of RNA device activity

Abstract

Recent advances have demonstrated the use of RNA-based control devices to program sophisticated cellular functions; however, the efficiency with which these devices can be quantitatively tailored has limited their broader implementation in cellular networks. Here, we developed a high-efficiency, high-throughput, and quantitative two-color FACS-based screening strategy to support the rapid generation of ribozyme-based control devices with user-specified regulatory activities. The high-efficiency of this screening strategy enabled the isolation of a single functional sequence from a library of over 10^6 variants within two sorting cycles. We demonstrated the versatility of our approach by screening large libraries generated from randomizing individual components within the ribozyme device platform to efficiently isolate new device sequences that exhibit increased catalytic activity up to 6.8-fold and increased activation ratios up to 160%. We also established a correlation between *in vitro* cleavage rates and *in vivo* gene-regulatory activities, supporting the importance of optimizing RNA device activity directly in the cellular environment. We further demonstrated the utility of the generated devices to regulate cell fate determination through a MAPK pathway associated with the mating response in yeast, highlighting our two-color FACS-based screen as an important strategy in quantitatively tailoring genetic control devices for broader integration within biological networks.

2.1 Introduction

The engineering of biological systems that exhibit complex functions has significant potential to develop solutions addressing global challenges spanning health and medicine, sustainability, and the environment (1-4). Core to the engineering of biological systems is the ability to process information within cellular networks and link this information to new cellular behaviors. Synthetic biology is a rapidly growing interdisciplinary field that involves the application of engineering principles to support the scalable construction and design of complex biological systems. One key focus of synthetic biology is to develop engineering frameworks for the reliable construction of genetic control devices that process and transmit information within living systems. Such information processing capabilities will allow researchers to implement diverse cellular control strategies, thus laying a critical foundation for designing genetic systems that exhibit sophisticated biological functions.

RNA control devices represent an important class of synthetic genetic control devices, whose development has been fueled by advances in RNA biology, engineering, and nucleic acid computing (5-9). We recently described a modular ligand-responsive ribozyme-based platform that supports efficient tailoring of RNA device function (10). The ribozyme device platform specifies physical linkages between three functional RNA components: a sensor encoded by an RNA aptamer, an actuator encoded by a hammerhead ribozyme, and a transmitter encoded by a sequence that undergoes a strand-displacement event (Figure 2.1). The dynamic range of an RNA control device, defined as the difference between gene expression levels in the presence and absence of ligand, is commonly described by two key parameters: basal activity and activation ratio. The basal

activity is a measure of regulatory stringency, which is set by the gene expression level in the absence of the input ligand, whereas the activation ratio is a measure of input responsiveness, which is set by the ratio of expression level in the presence to that in the absence of input ligand. The dynamic range exhibited by an RNA control device is important for its effective integration within biological systems. We have previously demonstrated a rational device tuning strategy guided by secondary structure predictions from an RNA folding program to direct the partitioning between the two functional device conformations (10). While we demonstrated the generation of a series of devices that span wide regulatory ranges, this strategy relies on predictions made by RNA folding programs, which base their computations on parameters acquired *in vitro*, and thus do not fully capture the complex RNA folding process *in vivo*. Therefore, an alternative strategy that enables more direct engineering of device dynamic ranges in the cellular environment is desired to increase the efficiency with which RNA devices can be tailored to cellular networks.

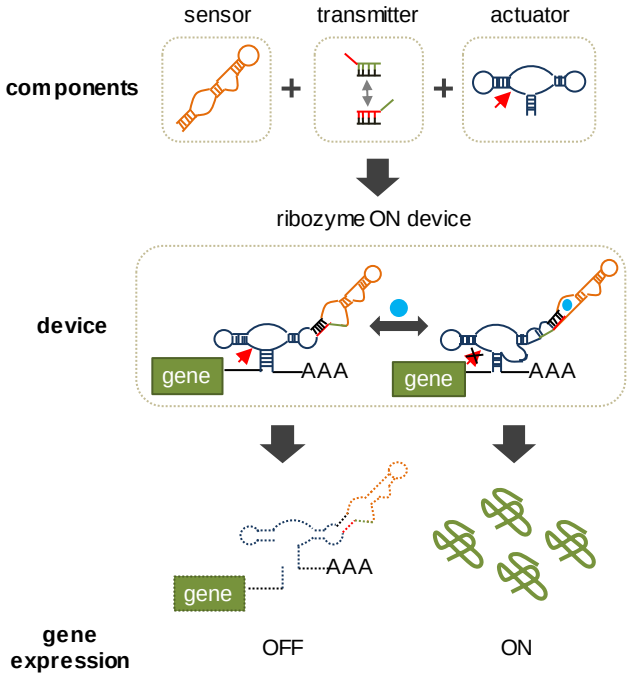

Figure 2.1 Schematic representation of modular assembly and mechanism of an RNA control device based on a ribozyme actuator. Ribozyme-based devices are constructed by modular assembly of three functional RNA components. A sensor (RNA aptamer) is linked to an actuator (hammerhead ribozyme) through a distinct information transmitter sequence (which directs a strand-displacement event and insulates the sensor and actuator components). Ribozyme-based devices are integrated into the 3' untranslated region (UTR) of the target gene and can adopt at least two functional device conformations, where each conformation is associated with different actuator and sensor activities. In the depicted example, a ribozyme ON device (up-regulation of gene expression in response to increased input ligand concentration) adopts a ribozyme-active conformation associated with an aptamer ligand-unbound state, where ribozyme cleavage results in an unprotected transcript that is subject to rapid degradation by ribonucleases, thereby leading to a decrease in gene expression. The ribozyme-inactive conformation is associated with an aptamer ligand-bound state, such that ligand binding to the aptamer stabilizes the ribozyme-inactive conformation, thereby leading to an increase in gene expression in response to ligand.

Significant research efforts have been directed toward developing high-throughput *in vitro* and *in vivo* selection and screening strategies to generate RNA control devices with user-specified regulatory activities. *In vitro* selection strategies were applied to allosteric ribozymes to select for variants that exhibit enhanced ligand-responsive

cleavage activities (11,12). However, in one case the selected variants did not retain their enhanced activities *in vivo*, suggesting that the observed activities were sensitive to the environment in which the selection was performed (11). To address potential loss of activities in transitioning between *in vitro* and *in vivo* environments, researchers have developed cell-based selection and screening strategies to support direct generation of RNA control devices and regulatory components in the relevant environment.

A cell-based selection strategy was developed to select for more active ribozyme variants by directly recovering cleaved ribozyme fragments from cells (13). However, this *in vivo* method decoupled cleavage activity from gene-regulatory activity, resulting in a less quantitative selection strategy that did not support effective identification of sequence variants with varying gene-regulatory activities. Cell-based screening and selection strategies have been developed for RNA control devices by introducing a randomized region into the device and linking the regulatory function of the resulting device library to a single measurable gene expression output, such as colorimetric and fluorescence levels (14-16), motility (17), or viability (18). However, the majority of these methods are most effective at enriching devices from the population exhibiting extreme (either low or high) gene expression levels, limiting the recovery of devices with specific quantitative activities. In addition, the enrichment efficiencies (or, alternatively, the throughput) of screening methods based on a single output can be negatively impacted by the stochastic nature of gene expression. In particular, when utilizing high-throughput methods that measure activities within single cells, such as fluorescence-activated cell sorting (FACS), the inability to resolve changes in gene expression activity

as a result of the genetic control device from cellular noise make single-output strategies less efficient and quantitative.

In this work, we developed a new screening strategy that utilizes two measurable outputs to resolve device regulatory activity from cellular noise. A high-efficiency, high-throughput, and quantitative two-color FACS-based screening strategy was developed to support rapid generation of RNA control devices with user-specified regulatory activities. We validated the high-efficiency of our screening strategy by performing a control sort to isolate the original functional sequence from a library over 10^6 variants within just two sorting cycles. We demonstrated the versatility of our two-color FACS-based approach by screening large libraries generated from randomizing individual components within the ribozyme device platform to efficiently isolate devices with improved regulatory properties. Using this screening strategy we effectively isolated new ribozyme actuator sequences that increase catalytic activity up to 6.8-fold within the device platform and new transmitter sequences that increase activation ratios up to 160%. By generating variants of RNA components with varying quantitative activities, the *in vivo* device screening approach was used to elucidate sequence-function relationships of RNA components and relationships between ribozyme cleavage rates and gene-regulatory activities. Last, we applied a newly generated device from our screens to control the expression of a key component in a MAPK pathway associated with the mating response in yeast. The new device with improved regulatory stringency allowed for robust rerouting of the mating phenotype in response to a small molecule input. These results highlight the utility of our two-color screen in tailoring the quantitative regulatory

properties of RNA devices to support more effective programming of complex cellular behaviors.

2.2 Results

2.2.1 A two-color reporter construct supports a high-efficiency, high-throughput, quantitative, cell-based screening strategy

Genetic control devices with desired regulatory activities are often generated through cell-based screening strategies by coupling the regulatory function to a measurable output. However, the efficiencies of high-throughput cell-based screening strategies based on measuring activities in single cells are negatively impacted by gene expression noise that arises from both extrinsic (e.g., cell size and shape, cell cycle stage, plasmid copy number) and intrinsic (e.g., fluctuation in numbers of DNA, RNA, transcription factors, environmental stimuli) factors (19,20). To develop a more effective and quantitative *in vivo* screening strategy for gene-regulatory devices, we constructed a screening plasmid composed of two independent functional modules (Figure 2.2A). The first module, the device activity reporter, utilizes a GFP reporter to measure the gene expression activity associated with the regulatory device, whereas the second module, the noise reporter, utilizes a mCherry reporter to provide a measure of cellular gene expression activity that is independent of the regulatory device. We used the same constitutive promoter (TEF1) in each module, although other promoter pairs may be substituted into the construct as previous studies in yeast suggest that extrinsic noise, which is the predominant source of gene expression noise, is not promoter specific (20).

Different terminators for each module were used to decrease the frequency of homologous recombination between the two modules.

We first used the two-color screening construct to examine the basal activities of three previously characterized theophylline-responsive ribozyme-based devices (10) based on the output from the device activity reporter (GFP): L2bulge1 (L2b1), 40%; L2bulge5 (L2b5), 70%; and L2bulge8 (L2b8), 11%. The reported basal activities refer to the GFP expression levels relative to that of the inactive ribozyme control in the absence of theophylline. While these three devices exhibit a wide range of regulatory activities, cellular noise results in a broad distribution of GFP fluorescence levels, making it challenging to cleanly isolate members with target activities from a library through a FACS-based sorting strategy based solely on one output (Figure 2.2B, C). To provide a filter for changes in gene expression activity due to cellular noise, we used the noise reporter in the two-color screening construct to assess activity that is independent of the regulatory device. By using the output from the noise reporter (mCherry), we were able to normalize the gene expression activities of individual cells by correlating the outputs between the two reporters and cleanly resolve the cell populations harboring three different devices (Figure 2.2D). For each device, the cell population exhibits a tight linear relationship between the two outputs, such that the device regulatory activity is associated with a distinct slope (Supplementary Figure S2.1). The increased resolution between cell populations harboring devices with different regulatory activities enables the development of a high-efficiency, quantitative, two-color FACS-based screening strategy based on the output correlation between the two reporter modules (Figure 2.2E).

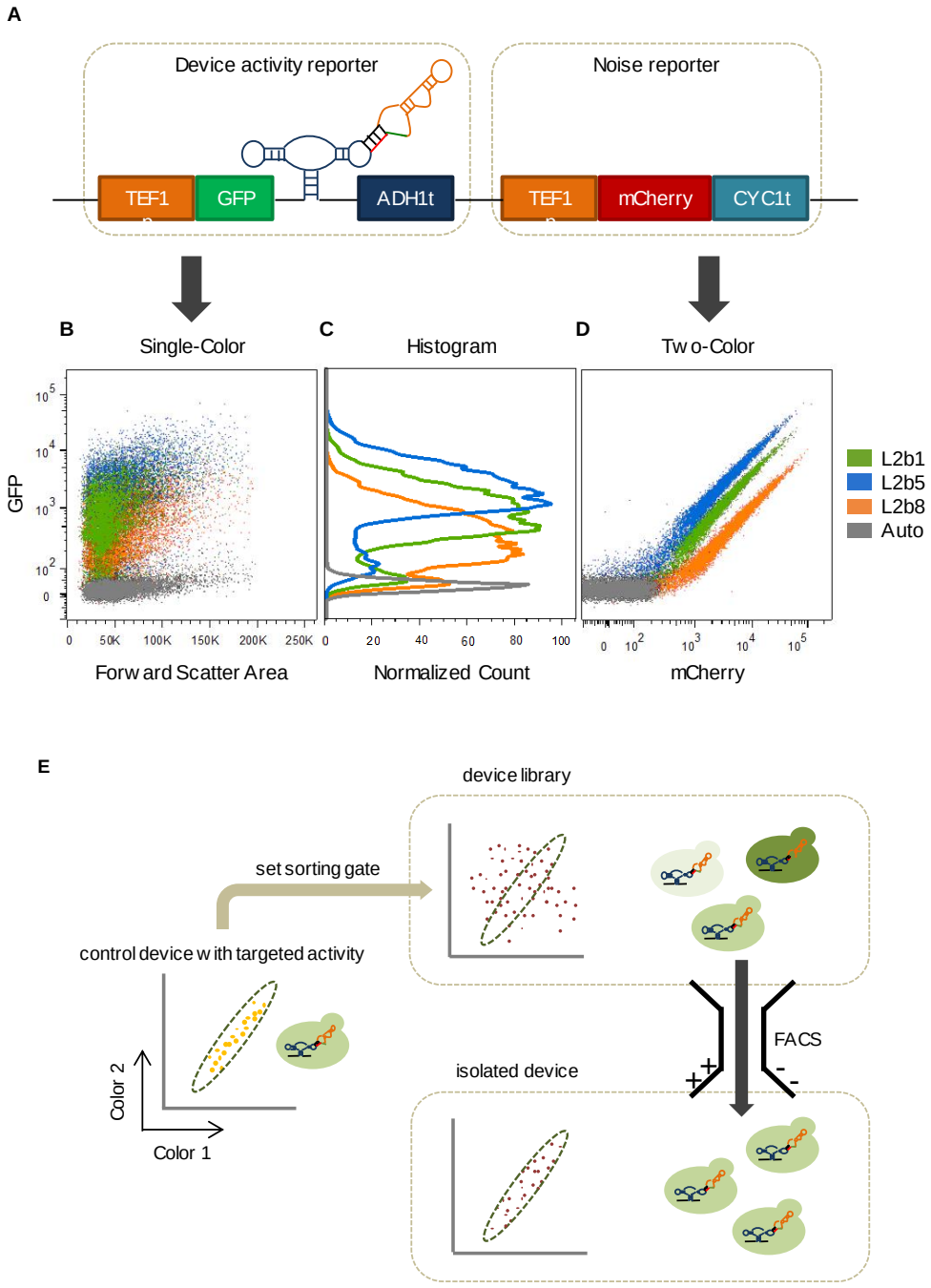

Figure 2.2 A high-efficiency, quantitative cell-based screening strategy for genetic devices based on a two-color screening construct. (A) The two-color screening construct is composed of two independent activity reporters. The device activity reporter measures the gene expression activity associated with the regulatory device from GFP fluorescence, whereas the noise reporter measures the cellular gene expression activity that is independent of the regulatory device from mCherry fluorescence. (B) Single-color (GFP)

scatter plots of three ribozyme-based devices that span a wide range of activities, as measured by their mean values, and cellular autofluorescence from a construct containing no fluorescence reporter gene exhibit significant overlap due to noise associated with gene expression. (C) Single-color (GFP) histograms illustrate that isolation of a device with a specific regulatory activity based on a single reporter output is inefficient due to overlapping population distributions. (D) The gene expression activities of individual cells can be normalized by correlating the device and noise reporter outputs from the two-color screening construct. Cell populations harboring the three ribozyme-based devices in (B) can be cleanly resolved on a two-color scatter plot, where each population exhibits a tight linear relationship between the two outputs. (E) The two-color screening strategy is based on the output correlation between the two reporter modules. A library of control devices can be integrated in the two-color screening construct and transformed into the target cell host. The sorting gate is set by the two-color correlation (slope) associated with a control device that exhibits desired activity and applied to the library to specifically isolate a cell population that exhibits similar activity (slope).

We demonstrated the high enrichment efficiency of our FACS-based two-color screening strategy by performing a control screen on a sensor library (sN10). The sN10 sensor library was generated by randomizing 10 nt positions in the theophylline aptamer binding core (sensor component) within the L2b8 device (~$1x10^6$ variants) (Figure 2.3A). We first assessed the basal activity of the sN10 sensor library through two-color flow cytometry analysis and observed that the majority of the library exhibits higher activity (greater slope) than the parent device (Figure 2.3B). We set a sorting gate based on the basal activity of the parent device (negative gate) and performed a negative sort to enrich cells (~10% of the initial library) that exhibit similar basal activities (same slope). We calculated the fold enrichment based on the percentage of the cell population isolated from each sort. In the initial negative sort, we collected 9.53% of the cell population and therefore this population was enriched ~11 times (100/9.53, or ~11-fold) for the subsequent screen. We performed a positive sort on the recovered cells, in which the lower bound of the sorting gate was set by the activity of the L2b8 device in the presence of 5 mM theophylline. The positive sorting gate was expanded further to enrich members

of the library (~7% of the enriched library) that exhibit equal or increased activities in response to theophylline relative to the parent device by ~15-fold. After one sorting cycle, a distinct small sub-population of cells that exhibit comparable basal activity to the parent device was observed. We then performed another round of sorting to specifically enrich this sub-population (~1% of the enriched library) through a negative sort by ~143-fold, followed by a positive sort on the recovered cells to enrich a clearly distinct cell population that exhibits increased gene expression activity (~4% of the enriched library) in response to theophylline by ~25-fold. After two sorting cycles, ~80% of the enriched library exhibits a clear population shift in response to theophylline (Figure 2.3C).

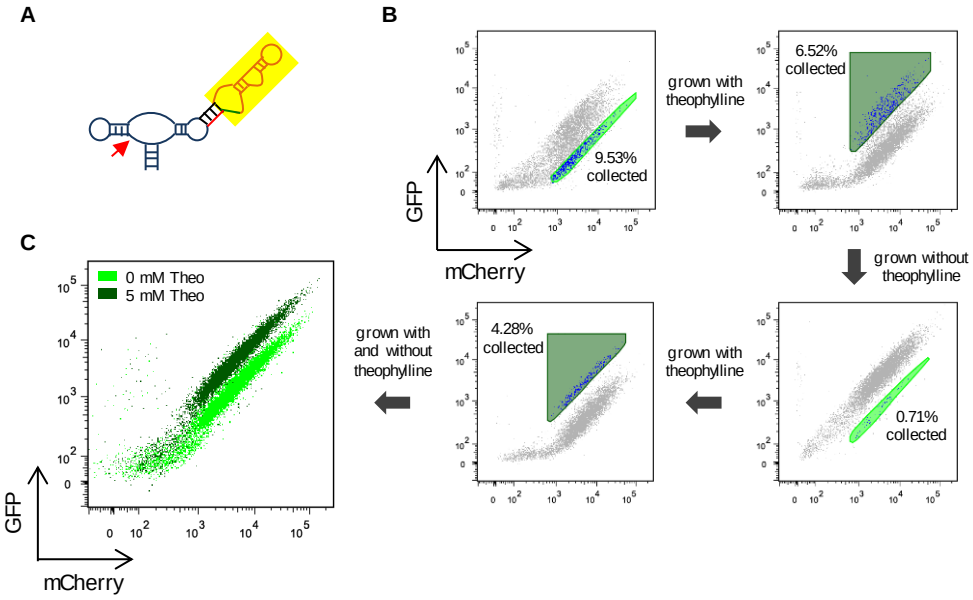

Figure 2.3 Screening of a sensor library within the device platform demonstrates the high enrichment efficiency of the two-color sorting strategy. (A) A sensor library, sN10, is generated by randomizing 10 nts at key positions within the aptamer component in a previously engineered theophylline-responsive ribozyme-based device, L2b8. (B) The sN10 library is subjected to two sorting rounds. Each round consists of one negative sort in the absence of theophylline (light green gate set by the activity of the parent L2b8 device in the absence of theophylline), followed by one positive sort in the presence of theophylline (dark green gate set by the activity of the parent L2b8 device in the presence

of 5 mM theophylline). Percentage of cells collected in the sorting gate is indicated on each plot. (C) After two sorting rounds, ~80% of the enriched sensor library exhibits a clear population shift in response to theophylline (theo).

Since the two rounds of sorting yield an overall ~6×10^5-fold enrichment, given an initial library diversity of ~10^6 variants we expected to recover the original parent device from the enriched library by screening a small number of individual clones. We characterized 48 individual colonies from the enriched library for increased theophylline-responsive activities through flow cytometry. All 48 colonies exhibit similar increases in GFP expression levels in response to theophylline as the parent L2b8 device. We sequenced the recovered devices from 10 colonies, and all were verified to be the parent sequence. These results demonstrate the high efficiency of our two-color FACS-based screening strategy, which can enrich a single sequence from a large ~10^6 library to close to pure isolation in as few as two sorting rounds. The efficiency of our screening strategy is a direct result of the high resolving power of our two-color screening construct. For example, when examining the enriched library after one round of sorting, we could observe a distinct cell population that exhibits comparable basal activity to the parent L2b8 device on a two-color scatter plot (Supplementary Figure S2.2). However, when examining the cell population on a single-color (GFP) histogram, noise associated with the gene expression activity results in poor resolution between the device regulatory activity and cellular noise, thereby significantly decreasing the enrichment efficiency of a screening strategy based on a single output.

2.2.2 Screening of an actuator library results in RNA control devices with improved regulatory stringencies

The implementation of RNA control devices in biological systems requires flexible tailoring of regulatory functions, where regulatory stringency of a device can be an important property for crossing phenotypic thresholds (1). The basal activity of a single ribozyme-based device depends on both the actuator and transmitter components. The catalytic activity of the hammerhead ribozyme (actuator) within the context of the device platform sets a lower limit to the minimal gene expression level a device exhibits in the absence of ligand, whereas the transmitter directs the partitioning between the functional conformations, which in turn impacts the basal activity (10). The device platform specifies the integration of a sensor-transmitter element through loop II (or loop I) of the satellite tobacco ringspot virus (sTRSV) ribozyme actuator. Previous sTRSV ribozyme characterization studies have demonstrated that a tertiary interaction between loop I and loop II is essential for the catalytic activity of the ribozyme in cellular environments (21). The integration of additional structural elements through the ribozyme loops may negatively impact the required loop-loop interaction, thus resulting in a less active ribozyme within the device platform. The previously described theophylline-responsive ribozyme devices (L2b1, 40%; L2b5, 70%; L2b8, 11%) exhibit a basal expression activity higher than that exhibited by the ribozyme alone (1%) (Supplementary Figure S2.3), suggesting that the current natural ribozyme sequence in the device platform may limit our ability to generate RNA control devices that exhibit tighter regulatory stringencies.

We focused initially on optimizing the sTRSV ribozyme sequence in the L2b8 device as it has the lowest basal activity among the series of previously engineered theophylline-responsive devices (10). As prior sTRSV ribozyme characterization studies

have demonstrated that mutations to either loop I or II sequences can enhance or hinder ribozyme cleavage activity (21), we designed a device library by randomizing loop sequences and applied our two-color FACS-based screening approach to search for improved loop-loop interactions that support lower basal activity. We generated an actuator library (aN7) by randomizing 7 nts in loop I within the L2b8 device (~$2x10^4$ variants) (Figure 2.4A). Loop I was targeted for randomization as it is isolated from the conformational change that is facilitated by the transmitter component, which is integrated via loop II. We analyzed the initial aN7 actuator library by two-color flow cytometry analysis and observed that ~99% of the library exhibits a higher basal activity (greater slope) than the parent L2b8 device, indicating that the majority of loop I library sequences have deleterious effects on ribozyme catalytic activity (Figure 2.4B). The two-color approach also enables us to clearly distinguish cells with low gene expression activity from cells that have lost or mutated the plasmid, whereas the two cell populations are almost indistinguishable if GFP is used as the only measure of device regulatory activity (Supplementary Figure S2.3). We set a sorting gate based on cells harboring the parent L2b8 device and collected cells that exhibit a decreased slope relative to the parent device (~0.4% of the initial library) to enrich library members with enhanced loop-loop interactions that support lower device basal activity.

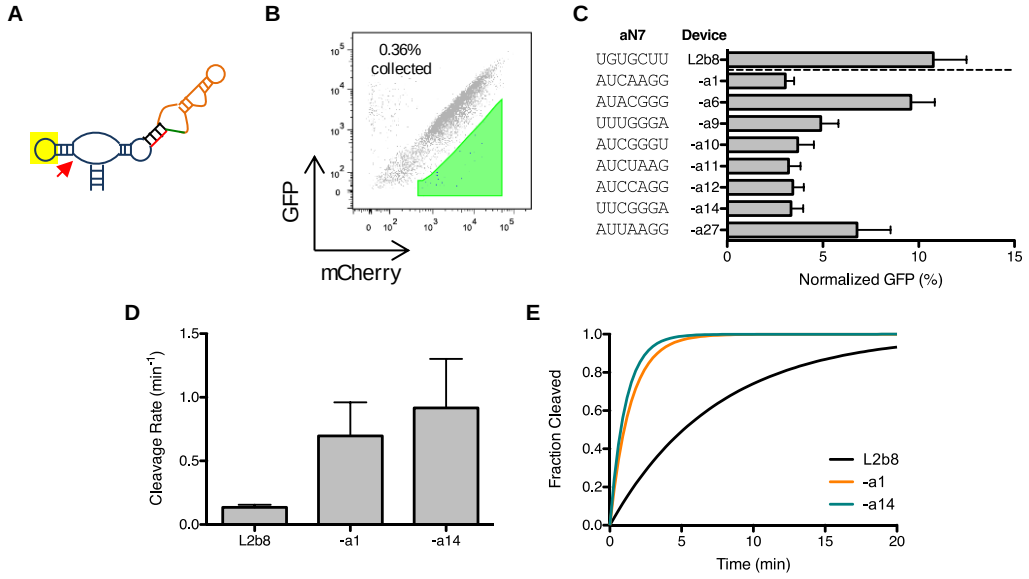

Figure 2.4 Screening of an actuator library within the device platform results in ribozyme variants that exhibit improved gene-regulatory stringencies and cleavage rates. (A) An actuator library, aN7, is generated by randomizing 7 nts at key positions within the loop I region of the ribozyme actuator in the L2b8 device. (B) The aN7 library is subjected to a single sort to enrich for devices that exhibit lower basal gene expression levels than the parent L2b8 device. The majority (~99%) of the aN7 library exhibits a greater slope than that of the parent L2b8 device, such that one sort is sufficient to isolate members that exhibit improved regulatory stringency. (C) Ribozyme variants isolated from the aN7 library screen exhibit lower basal activities relative to the parent L2b8 device. Gene-regulatory activities are reported as the geometric mean of the GFP fluorescence of the indicated sample normalized to that of a positive control (sTRSV Contl, a noncleaving sTRSV ribozyme with a scrambled core) that is grown under identical ligand conditions and is set to 100%. Reported values are the mean and standard deviation of at least three independent experiments. (D) The recovered ribozyme variants (L2b8-al, -a14) exhibit faster cleavage rates than the parent device (L2b8). Cleavage assays were performed at 37˚C with 500 μM $MgCl_2$, 100 mM NaCl, 50 mM Tris-HCl (pH 7.0). Cleavage rate constants (k) and errors are reported as the mean and standard deviation from at least three independent assays. (E) *In vitro* cleavage kinetics of the ribozyme variants (L2b8-al, -a14) and the parent device (L2b8). The projected cleavage kinetics are generated from the single-exponential equation $F_t = F_0 + (F_\infty - F_0)\times(1 - e^{-kt})$, setting the fraction cleaved before the start of the reaction (F_0) and at reaction endpoint (F_∞) to 0 and 1, respectively, and k to the experimentally determined value for each RNA device.

Due to the relatively small sequence space of the library and high-efficiency of our screen, we directly plated the sorted cells to obtain single colonies for further

characterization. We recovered a total of 22 clones and identified 22 unique device sequences from the recovered clones. However, only eight of the recovered devices maintained low basal activities upon re-cloning (Figure 2.4C), while the remaining devices likely had mutations within the recovered plasmid backbone. The basal activities exhibited by the recovered devices are up to 3.5-fold lower than that of the parent device, while five of the devices retained functional switching (i.e., responsiveness to ligand) (Supplementary Figure S2.4).

We performed a sequence analysis to identify the loop I sequence requirements that support high ribozyme catalytic activity within the device platform. A series of point mutations to the recovered loop I sequences were designed, and the activities of these loop I sequences were characterized through flow cytometry analysis (Supplementary Figure S2.5). Two distinct consensus sequences were identified that support lower basal activities than the parent L2b8 device. RNA devices with a loop I heptaloop adhering to the consensus sequence AUNNRRG, where N is any nucleotide base and R is a purine base, exhibit basal activities that are less than or equal to that of the parent (11%). A subset of these devices with the loop I consensus sequence AU(C/U/G)NARG exhibit basal activities less than 80% of that of the L2b8 parent device. Further restricting the loop I consensus sequence to AUCNARG results in additional improvements to the basal activity, to 40% of that of the parent. RNA devices with a second, distinct loop I consensus sequence predicted to form a triloop $N_1UN_2GGGN_1^{|}$, where N_1 and $N_1^{|}$ are any Watson-Crick base pair, exhibit improved basal activities less than 70% of that of the L2b8 parent.

2.2.3 Engineered actuator components result in optimized ribozyme-based devices exhibiting faster cleavage rates

In vitro kinetic analysis of select ribozyme-based devices harboring loop I sequence modifications was performed to assess whether the improved *in vivo* basal activities were a result of increased catalytic rate relative to the parent device. Cleavage rates (*k*) were determined at physiologically-relevant reaction conditions (500 μM $MgCl_2$, 100 mM NaCl, and 50 mM Tris-HCl (pH 7.0)) at 37°C, where the submillimolar magnesium concentration is within the range estimated for intracellular magnesium concentration (22). Cleavage rate constants were obtained for the L2b8 parent device and the L2b8-a1 and -a14 engineered devices (Figure 2.4D, E) by quantifying relative levels of full-length and cleaved radiolabeled transcripts through polyacrylamide gel electrophoresis analysis (Supplementary Figure S2.6). Compared to the cleavage rate constant of L2b8 (0.14 min^{-1}), the cleavage rates associated with the engineered devices are increased 5- and 6.8-fold for L2b8-a1 (0.70 min^{-1}) and -a14 (0.92 min^{-1}), respectively. The cleavage rate of the sTRSV hammerhead ribozyme (4.3 min^{-1}) was determined at these conditions to be 45-fold greater than L2b8 (Supplementary Figure S2.6), in agreement with prior analyses on this ribozyme (21) and other well characterized natural ribozymes under physiologically relevant conditions (23). The results indicate that the modified loop I sequences produce ribozyme-based devices exhibiting faster cleavage rates and thus lower basal expression levels.

2.2.4 Screening of transmitter libraries results in RNA devices exhibiting improved activation ratios

The dynamic range of an RNA control device depends on many parameters, including irreversible rate (e.g., ribozyme cleavage activity), intracellular ligand concentration, and mechanism by which binding information at the sensor is transmitted to an activity change in the actuator (e.g., transmitter design). We applied our two-color FACS-based screening strategy to explore a greater functional space to search for new transmitter sequences that support improved activation ratios given the designated sensor and actuator component pairs. We generated two transmitter libraries, tN11 and a1-tN11, based on two theophylline-responsive ribozyme-based devices, L2b8 and L2b8-a1, respectively, with ribozyme components that exhibit varying catalytic activities. Both libraries were generated by randomizing 11 nts in the transmitter component within the corresponding parent device (~$4x10^6$ variants) (Figure 2.5A). We limited the number of randomized nucleotides in the transmitter components to result in libraries that could be completely searched based on the efficiency of our yeast library transformation method (see Materials and Methods). Both libraries were screened to identify devices with comparable basal activities but with greater activation ratios relative to the corresponding parent devices (Figure 2.5B, D). We first performed a negative sort on both libraries by setting the sorting gates based on the basal activity of the respective parent device. The negative sort enriched members of the library (~3% of the initial tN11 library; ~5% of the initial a1-tN11 library) that exhibit lower or comparable basal activities as the parent device. A subsequent positive sort was performed on the recovered cell populations by setting sorting gates based on the gene expression activity of the respective parent device

in the presence of 5 mM theophylline. To enrich members of the library that exhibit improved activation ratios, cells that exhibit equal or higher gene expression activities (~0.3% of the enriched tN11 library; ~0.4% of the enriched a1-tN11 library) were isolated. One additional positive sort was performed on the enriched tN11 library to further enrich for cells that exhibit activation ratios greater than or equal to the parent device (~24% of the enriched library).

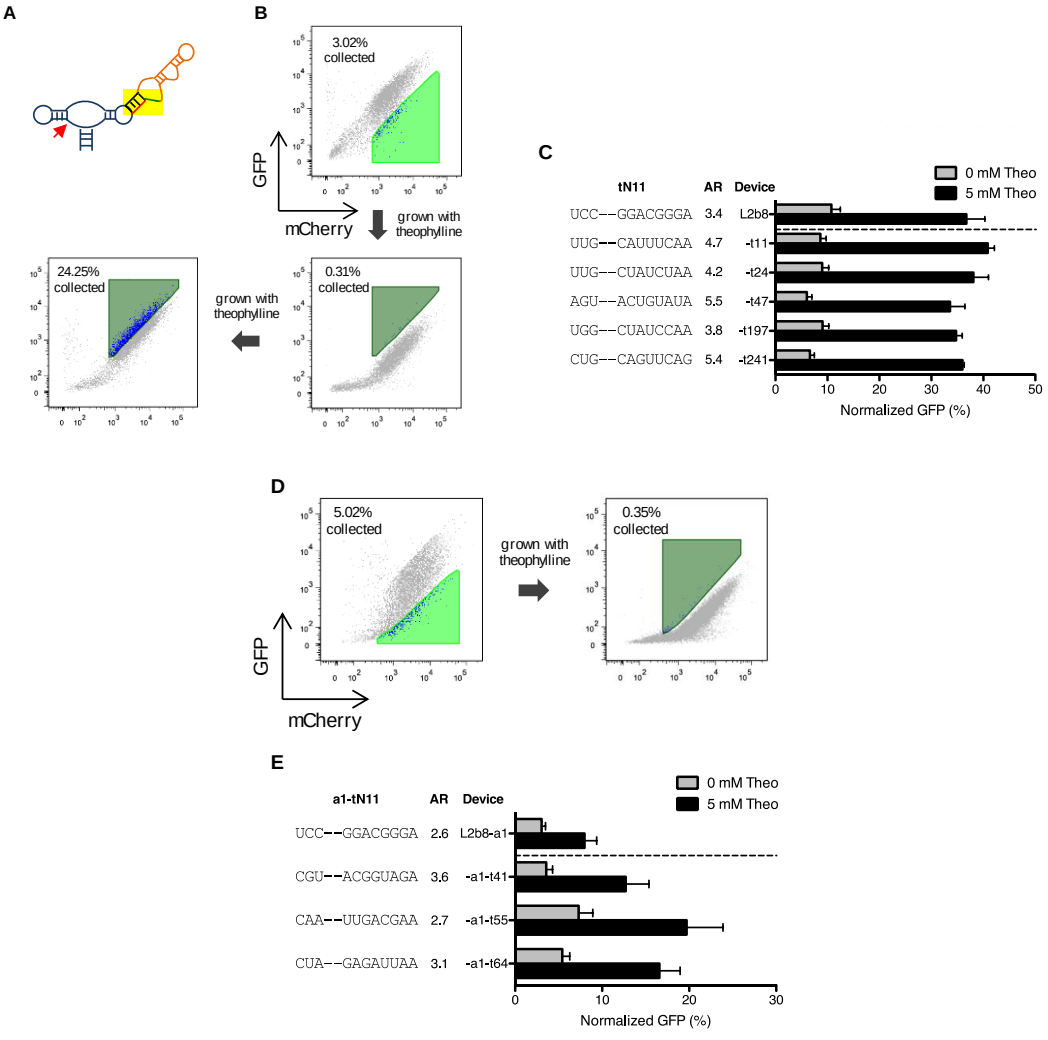

Figure 2.5 Screening of transmitter libraries within the device platform results in transmitter variants that exhibit improved activation ratios. (A) Two transmitter libraries, tN11 and a1-tN11, are generated by randomizing 11 nts within the transmitter components in the L2b8 (wild-type ribozyme actuator) and L2b8-a1 (enhanced ribozyme actuator) devices, respectively. (B) The tN11 library is subjected to one sorting round (negative and positive sort), followed by an additional positive sort to further enrich members of the library that exhibit equal or greater increases in gene-regulatory activities in response to theophylline. The negative (light green) and positive (dark green) sorting gates are set based on the activity of the parent L2b8 device in the absence and presence of 5 mM theophylline, respectively. (C) Transmitter variants isolated from the tN11 library screen exhibit improved activation ratios. Gene-regulatory activities are reported as described in Figure 2.4C. Reported values are the mean and standard deviation of at least three independent experiments. The activation ratio (AR) is determined as the ratio of gene expression levels in the presence and absence of theophylline. (D) The a1-tN11 library is subjected to one sorting round to enrich members of the library that exhibit equal or greater increased in gene-regulatory activities in response to theophylline. The negative (light green) and positive (dark green) sorting gates are set based on the activity of the parent L2b8-a1 device in the absence and presence of 5 mM theophylline, respectively. (E) Transmitter variants isolated from the a1-tN11 library screen exhibit improved activation ratios. Gene-regulatory activities are reported as described in Figure 2.4C. Reported values are the mean and standard deviation of at least three independent experiments.

We plated the recovered cells from both final enriched libraries and screened 287 and 207 individual colonies from the tN11 and a1-tN11 libraries, respectively, through flow cytometry in the absence and presence of 5 mM theophylline and verified improved device activation ratios by re-cloning. We identified a total of five (t11, t24, t47, t197, t241) and three (a1-t41, a1-t55, a1-t64) transmitter variants from the tN11 and a1-tN11 library screen, respectively, that exhibit moderately improved activation ratios up to 160% relative to the parent devices (Figure 2.5C, E). We speculated that the intracellular theophylline concentration in yeast might limit the maximum activation ratio achievable by a device, as previous studies have estimated an 1000-fold drop in theophylline concentration across the *Escherichia coli* cell membrane (24). We tested this hypothesis by characterizing the activation ratios of the transmitter variants at a higher theophylline

concentration (40 mM) and observed devices with activation ratios up to 10.7-fold, corresponding to up to a 290% improvement in activation ratios relative to 5 mM theophylline (Supplementary Figure S2.7, S2.10). No difference in cell viability was observed under all theophylline conditions tested (Supplementary Figure S2.8A), although the higher theophylline concentration resulted in slower cell growth, possibly due to the ligand cytotoxicity, thus potentially rendering the implementation of these devices at higher ligand concentrations less effective for cellular applications.

2.2.5 Modular assembly of optimized actuator components results in devices exhibiting improved regulatory stringencies

The modular composition framework of our ribozyme device platform supports modular assembly of functional RNA components to generate new device functions without significant redesign (10,25). We examined the ability of the optimized ribozyme sequences to be used to build new device regulatory functions, by coupling two of the recovered ribozyme variants (a1, a14) with different sensor and transmitter components. We coupled the new actuator sequences with the transmitter and sensor components from two theophylline-responsive ribozyme ON devices (L2b1, L2b5), one theophylline-responsive OFF device (L2bOFF1), and one tetracycline-responsive ON device (L2b8tc) to generate eight new devices. All newly generated devices exhibit lower basal activities relative to their respective parent, and the majority of them retain switching activity (Supplementary Figure S2.9A-D). The ribozyme variants were also coupled with selected transmitter variants to generate new functional devices with varying regulatory stringencies and activation ratios (Supplementary Figure S2.10). The results indicate that

the improved ribozyme variants are relatively insensitive to the sequence identities of the other device components (transmitter, sensor) and highlight that the modular device platform can be used in combination with improved components to program RNA devices exhibiting desired activities. Finally, we examined the activities of the loop sequences outside of the device context by replacing the wild-type loop I sequence of sTRSV to generate two ribozyme variants (Supplementary Figure S2.9E). The gene expression activities of the resulting ribozyme variants were substantially higher than that of wild-type sTRSV, indicating that the improvement in regulatory stringencies associated with these loop sequences were specific to the context of the device platform, thus supporting the importance of optimizing component functions directly within the device platform.

2.2.6 *In vitro* cleavage kinetics reflect *in vivo* RNA device gene-regulatory activities

The observation that loop I modified ribozyme-based devices exhibit improved *in vivo* basal activities and *in vitro* cleavage rates relative to the L2b8 parent device suggests a correlation between these two measures of activity. However, previous studies had shown that allosteric ribozymes exhibiting enhanced *in vitro* cleavage rates through *in vitro* selections failed to exhibit enhanced *in vivo* gene-regulatory activities (11). Therefore, we examined the relationship between *in vitro* cleavage rates and *in vivo* gene-regulatory activities for a set of RNA devices generated through the two-color screening and rational tuning strategies. Cleavage assays were performed under the previously described physiologically-relevant reaction conditions in the absence and presence of 5 mM theophylline (Supplementary Figure S2.6). The ribozyme-based devices exhibit

cleavage rates that span approximately two orders of magnitude from 0.01 min^{-1} (L2b5) to 1.0 min^{-1} (L2b8-a1, a14) (Figure 2.6A, B). Nearly all of the examined RNA devices exhibit reduced cleavage rates in the presence of theophylline, except for L2b8-a14, which did not exhibit changes in gene-regulatory activity in response to theophylline (Supplementary Figure S2.4). The rank ordering of the examined RNA devices and the sTRSV ribozyme control by *in vitro*-determined cleavage rates matches the inverse ranking by *in vivo* gene-regulatory activities (Figure 2.6C). A correlation analysis between these two measures of activity indicates a strong negative correlation (Pearson coefficient, r = -0.9018) between the cleavage rates 0.007 and 0.16 min^{-1}, where at a cleavage rate of 0.16 min^{-1} near background levels of gene expression are reached such that further decreases in gene-regulatory activity are not observed with faster cleavage rates.

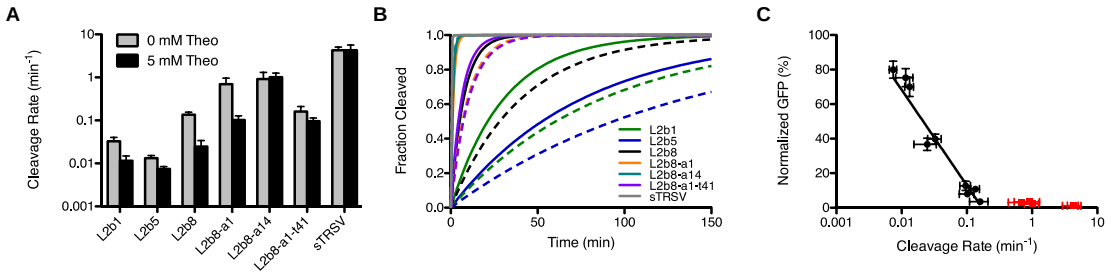

Figure 2.6 *In vitro* cleavage kinetics of selected ribozyme-based devices and controls. Cleavage assays were performed at 37˚C with 500 μM $MgCl_2$, 100 mM NaCl and 50 mM Tris-HCl (pH 7.0) and in the presence of 5 mM theophylline when indicated. (A) Ribozyme-based devices exhibit decreased cleavage rates in the presence of ligand. Cleavage assays were performed as described in Figure 2.4D in the absence or presence of 5 mM theophylline. (B) *In vitro* cleavage kinetics of ribozyme-based devices in the absence and presence of ligand. Projected cleavage kinetics are generated as described in Figure 2.4E. Solid lines: 0 mM theophylline; dashed lines: 5 mM theophylline. (C) Correlation analysis of normalized gene expression levels and cleavage rate constants indicates a strong correlation between the *in vivo* gene-regulatory activity and *in vitro* cleavage rate; Pearson correlation coefficient (r) of -0.9018. A semi-log line is well-fit (R^2 = 0.94) for cleavage rates less than or equal to 0.16 min^{-1} (black data points). Devices excluded from this analysis are indicated in red.

2.2.7 RNA control devices with improved regulatory stringency allow for robust redirecting of yeast mating fates

To achieve robust control of cell fate, the dynamic range of a genetic device must cross the threshold activity of the gene associated with the phenotypic change in the absence and presence of input molecule. RNA control devices have been integrated with biological systems to program complex cellular behaviors, such as proliferation and apoptosis (1,2). In these and other systems, devices with more stringent regulatory activities are necessary to sufficiently reduce background expression to achieve the desired control over the targeted phenotype. From our two-color FACS-based screens, we isolated new device variants that exhibit more than 3.5-fold lower basal activities relative to the parent device. To demonstrate the utility of devices with improved regulatory stringency, we applied these devices to control cell fate determination through a MAPK pathway associated with the mating response in yeast (Figure 2.7A).

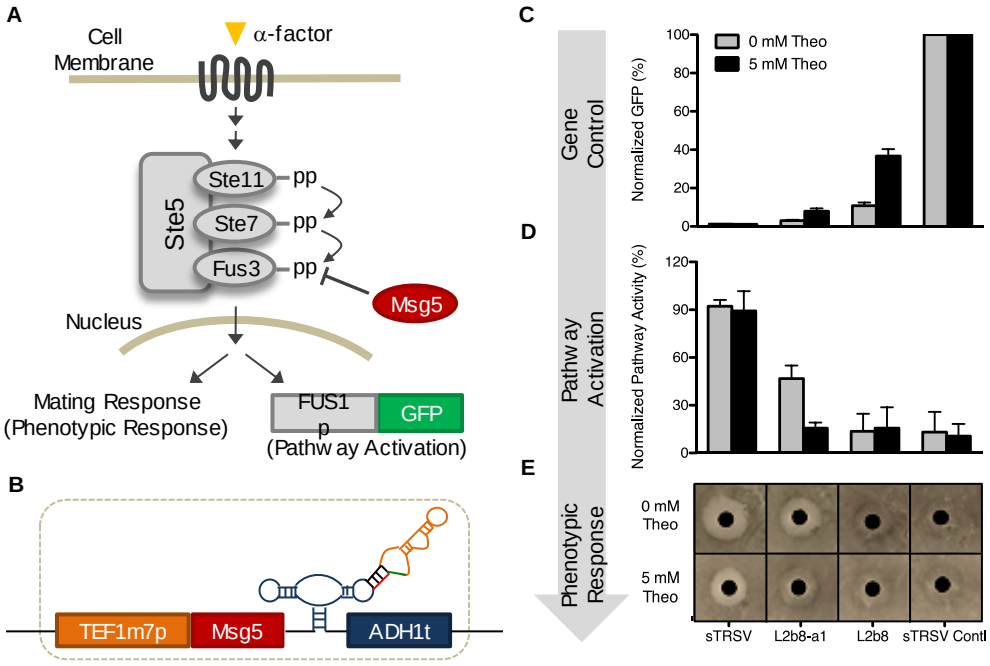

Figure 2.7 Fate routing in the yeast mating pathway with RNA devices. (A) Signaling through the yeast mating pathway starts with pheromone (α-factor) binding to a transmembrane receptor. Receptor binding is transmitted to the scaffold-bound canonical three-tiered MAPK cascade via a phosphorylation relay. Msg5 antagonizes signaling by dephosphorylating Fus3. Translocation of the phosphorylated MAPK, Fus3, to the nucleus initiates transcription at mating genes. Pathway activation is indicated by increased GFP levels (from a transcriptional fusion to the mating-responsive promoter FUS1p) and cell cycle arrest (observed via halo assays). (B) Schematic representation of fate routing constructs, where ribozyme-based devices and controls are placed downstream of a TEF1m7p-Msg5 cassette. (C) Gene-regulatory activities of RNA devices and controls utilized to regulate the yeast mating pathway. Gene-regulatory activities are reported as described in Figure 2.4C. Reported values are the mean and standard deviation of at least three independent experiments. (D) Stringent control of a negative regulator component in the yeast mating pathway is necessary to regulate pathway activation. Normalized pathway activity is reported as the geometric mean of three biological replicates normalized to FUS1p-yEGFP3 expression in the absence of MSG5 expression, and error bars represent the standard deviation of the replicates. (E) Stringent control of a negative regulatory component in the yeast mating pathway is necessary to route cellular fate. Halo formation is a direct read-out of pheromone-induced cell cycle arrest, where reduced halo formation in the presence of pheromone indicates pathway inhibition. Notably, halo formation is inhibited for the systems implementing L2b8 and sTRSV Contl as controllers in the absence or presence of theophylline. In contrast, the system implementing L2b8-a1 exhibits normal halo formation in the absence of theophylline (comparable to sTRSV) and significantly reduces halo formation in the

presence of theophylline. Representative images from three biological replicates are shown.

We targeted a key negative regulator in the mating pathway, Msg5, which is a MAPK phosphatase that inactivates signaling through this pathway by dephosphorylating the MAPK Fus3 (26). We first examined the impact on cell fate by ectopically expressing Msg5 regulated by either the wild-type ribozyme (sTRSV) or the inactive ribozyme (sTRSV Contl) controls (Figure 2.7B, C). These two controls represent the minimal and maximal expression levels of Msg5 in our synthetic system, and the corresponding pathway activation was analyzed through a fluorescent reporter assay that measures transcriptional activation of the pathway and a phenotypic assay that measures cell cycle arrest in the presence of pheromone (Figure 2.7D, E). The low expression level of Msg5 associated with the sTRSV construct allowed pathway activation in the presence of the pheromone, thereby leading to high GFP levels and wild-type halo formation. In contrast, the high expression level of Msg5 associated with the sTRSV Contl construct inhibited pheromone-induced pathway activation, thereby eliminating cell cycle arrest and resulting in low GFP levels.

To redirect yeast mating behavior in response to an exogenously applied molecular input, we implemented two theophylline-responsive ribozyme ON devices, L2b8 and L2b8-a1, to conditionally regulate expression of Msg5 (Figure 2.7B, C). The L2b8 device exhibits the lowest basal expression activity (11%) among the devices previously engineered through a rational design strategy (10). However, the basal expression level of Msg5 associated with the L2b8 device inhibited pathway signaling sufficiently to eliminate cell cycle arrest in the presence of pheromone even in the

absence of theophylline (Figure 2.7D, E). In contrast, the newly selected L2b8-a1 device exhibits a more stringent control profile than that of the L2b8 device and when applied to the regulation of Msg5 achieved rerouting of cell fate in response to the small molecule input. In the absence of theophylline, the basal expression level of Msg5 associated with the L2b8-a1 device was sufficiently low to permit elevated pathway activity in response to pheromone and characteristic halo formation as is observed for the wild-type ribozyme control. In the presence of theophylline, the increased expression level of Msg5 inhibited pathway activation sufficiently to reduce pheromone-induced cell cycle arrest, diminishing the appearance of the halo as is observed for the inactive ribozyme control. These results highlight the importance of tunable controllers, including those exhibiting stringent profiles, in targeting thresholds of key pathway components to achieve desired phenotypic switching. Although the L2b8 device exhibits a greater activation ratio relative to that of the L2b8-a1 device (Supplementary Figure S2.4), the higher basal activity of the L2b8 device rendered it ineffective in redirecting cell fate in this system.

2.3 Discussion

We developed a two-color FACS-based screening approach that enables the efficient isolation of devices with targeted regulatory activities (enriching a single sequence from a large ~10^6 library to close to pure isolation in two sorting rounds), providing a substantial improvement over the enrichment efficiencies of more commonly used single output screening strategies that can be negatively impacted by noise associated with gene expression. We applied our two-color screening approach to optimize the actuator and transmitter components directly within the context of the

ribozyme device platform in the relevant cellular environment, thereby addressing challenges previously encountered with optimizing component activities through *in vitro* strategies (11). The highly quantitative nature of our screening approach allowed us to efficiently isolate ribozyme and transmitter variants that exhibit specified regulatory activities. Our two-color screening approach is also fully complemented by the modular composition framework of the ribozyme-based platform. We demonstrated a plug-and-play device construction strategy by linking components with varying activities to generate new RNA devices that span wide regulatory ranges. In comparison to the previously demonstrated computational-guided device tuning strategy, which is restricted to experimentally sampling a smaller sequence space, our two-color screening approach offers greater flexibility and higher-throughput in quantitatively tailoring device regulatory properties.

We further characterized the isolated ribozyme and transmitter variants in addition to the devices generated previously by rational design through both *in vivo* and *in vitro* assays and found a strong negative correlation between gene-regulatory activities and cleavage rates, for cleavage rates within the range of 0.007 and 0.16 min^{-1} (measured at the specified reaction condition of 500 μM $MgCl_2$). Gene expression levels reach background values at ~0.16 min^{-1}, such that that increases in cleavage rate above this value have minimal impact on expression levels. In addition, our analysis (Figure 2.6C) indicates that below cleavage rates of ~0.007 min^{-1} gene expression levels reach saturating (fully ON) levels, such that further decreases in cleavage rate below this value do not significantly impact gene expression. Our work demonstrates that there is a narrow window of *in vitro* cleavage rates (spanning less than two orders of magnitude) that

correspond to titratable *in vivo* gene-regulatory activities. This observation may explain previous work in the field that observed no changes in gene-regulatory activities between ribozyme variants exhibiting different cleavage rates, if the changes in cleavage rates were occurring outside of the titratable window (13).

Our results also highlight the importance of optimizing individual components within the context of device platforms. The parent actuator component (sTRSV ribozyme) is a type-III hammerhead ribozyme, in which the 5' and 3' ends of viroid RNA extend from stem III. The tertiary interactions essential for cleavage activity at physiological conditions are formed by a Watson-Crick base triple between the 5' U of loop I, next-to-last U of loop I, and the 3' A of loop II. Recent structural analyses have shown that these essential tertiary interactions are conserved across a significant fraction of natural hammerhead ribozymes (27). As the loop I sequence of the originally designed ribozyme-based devices, including the parent device L2b8, is unchanged from the native sTRSV ribozyme (UGUGCUU), it was assumed that aptamer integration into loop II would maintain the same tertiary interactions required for cleavage activity (10). However, both the heptaloop (AUCNARG) and triloop ($N_1UN_2GGGN_1'$) consensus sequences identified through the actuator library screen that result in devices exhibiting lower basal activities than the L2b8 parent device do not follow the common tertiary motif of the sTRSV ribozyme. The divergence of the improved loop I sequences from the L2b8 and sTRSV parents are not necessarily surprising, given recent work identifying thousands of new hammerhead ribozymes in all domains of life with unique tertiary motifs (27-29). In particular, the integration of the transmitter-aptamer element into loop II of the sTRSV hammerhead ribozyme in the device platform makes the overall structure of the

ribozyme-based devices more similar to other, less well-characterized hammerhead ribozymes (Supplementary Figure S2.11). Interestingly, the improved loop I consensus sequences identified in our screen share similarities to these other natural ribozymes and do not exhibit improved activities in the context of the sTRSV ribozyme alone.

Finally, we demonstrated the utility of our newly selected device variants to control the expression level of a key negative regulator in the yeast mating pathway through an exogenously applied molecular input. In this particular system, the regulated pathway component exhibits a low threshold level, thus requiring a regulatory device with low background activity to permit pathway activation in the absence of the effector molecule. We applied one of the selected device variants with improved regulatory stringency to achieve phenotypic switching in response to the exogenous molecular input, whereas the original device was ineffective in redirecting cell fate. These results highlight the importance of fine-tuning regulatory properties of gene-regulatory elements for their successful integration within biological systems. Recent examples have relied on using low-throughput and inefficient single-color screening strategies on individual clones from libraries of control elements, including promoters and RNase cleavage sites, to identify new elements that exhibit varying activities in different organisms (30-32). In contrast, our two-color FACS-based screening approach is based on the correlation between the gene outputs from two independent functional modules. Similar dual-reporter screening plasmid systems can be constructed in other organisms, including bacteria and mammalian cells, to support the efficient generation of new gene control elements, including those acting through transcriptional and posttranscriptional mechanisms. Our strategy offers a high-throughput and high-efficiency alternative to rapidly screen through

diverse libraries of control elements for members exhibiting specified quantitative activities, thereby addressing a key challenge in quantitatively tailoring these control elements to specific genetic systems.

2.4 Materials and Methods

2.4.1 Plasmid and strain construction

Standard molecular biology cloning techniques were used to construct all plasmids (33). DNA synthesis was performed by Integrated DNA Technologies (Coralville, IA) or the Protein and Nucleic Acid Facility (Stanford, CA). All enzymes, including restriction enzymes and ligases, were obtained through New England Biolabs (Ipswich, MA). Ligation products were electroporated with a GenePulser XCell (Bio-Rad, Hercules, CA) into an *E. coli* DH10B strain (Invitrogen, Carlsbad, CA), where cells harboring cloned plasmids were maintained in Luria-Bertani media containing 50 mg/mL ampicillin (EMD Chemicals, Philadelphia, PA). All cloned constructs were sequence verified by Elim Biopharmaceuticals (Hayward, CA).

The two-color screening plasmid pCS1748 (Supplementary Figure S2.12) was constructed by inserting an open reading frame (ORF) encoding a yeast-optimized mCherry gene (*ymCherry*) flanked by a TEF1 promoter and a CYC1 terminator upstream of the existing ORF encoding a yeast-enhanced GFP gene (*yEGFP3*) flanked by a GAL1-10 promoter and an ADH1 terminator in the pCS321 backbone (10). The TEF1 promoter was PCR amplified from pG2M (34) using forward and reverse primers SacI-TEF1-fwd (5’-GAGAGCTCAAGCTTCAAAATGTTTCTACTCC) and SacII-TEF1-rev (5’-GGCCGCGGCAAAACTTAGATTAGATTGCTATGC), respectively, and inserted into

pCS321 via the unique restriction sites SacI and SacII. The *ymCherry* gene was PCR amplified from BBa_E2060 obtained from the iGEM parts registry (35) using forward and reverse primers SacII-mCherry-fwd (5'-GACCGCGGGAAATAATGTCTATGGTTAGTAAAGGAGAAGAAAATAACATGGC) and NotI-mCherry-rev (5'-GGGCGGCCGCTTATTATTTGTATAGTTCATCCATGCCACCAG), respectively, and inserted downstream of the cloned TEF1 promoter via the unique restriction sites SacII and NotI. The CYC1 terminator was PCR amplified from pCM159 (36) using forward and reverse primers NotI-CYC1t-fwd (5'-GAGCGGCCGCGAGGGCCGCATCATGTAATTAG) and XbaI-CYC1t-rev (5'-GGTCTAGAGGCCGCAAATTAAAGCCTTCG), respectively, and inserted downstream of the cloned *ymCherry* gene via the unique restriction sites NotI and XbaI. A spacer sequence was amplified from pCS745 (gift from M. Jensen, Seattle Children's Research Institute) using forward and reverse primers XbaI-Spacer-fwd (5'-GGTCTAGACGCCTTGAGCCTGGCGAACAGTTC) and Spacer-rev (5'-AGTAAAAAAGGAGTAGAAACATTTTGAAGCTATCGATGACAGGATGAGGATCGTTTCGCATG), respectively. A TEF1 promoter fragment was amplified from pG2M using forward and reverse primers Spacer-TEF1-fwd (5'-CATGCGAAACGATCCTCATCCTGTCATCGATAGCTTCAAAATGTTTCTACTCCTTTTTTACT) and BamHI-TEF1-rev (5'-GGGGATCCCAAAACTTAGATTAGATTGCTATGCTTTCTTTC), respectively, and PCR assembled with the spacer fragment. The assembled spacer-TEF1 promoter fragment was inserted into the modified

pCS321 backbone to replace the GAL1-10 promoter via the unique restriction sites XbaI and BamHI.

Two single-color plasmids harboring GFP (pCS1585) and mCherry (pCS1749) were constructed as compensation controls for FACS analysis. A fragment harboring the TEF1 promoter was PCR amplified from pGM2 using forward and reverse primers SacI-TEF1-fwd (5'-GAGAGCTCATAGCTTCAAAATGTTTCTACTCC) and EcoRI-TEF1-rev (5'-GGGAATTCT TTGTAATTAAAACTTAGATTAGA), respectively. The GFP-only plasmid pCS1585 was constructed by inserting the TEF1 promoter fragment into pCS321 to replace the GAL1-10 promoter via the unique cloning sites SacI and EcoRI. The mCherry-only plasmid pCS1749 was constructed by inserting the TEF1p-ymCherry–CYC1t cassette from pCS1748 into a modified version of pRS316 (37) via the unique restriction sites SacI and XbaI. The modified version of pRS316 (pCS4), containing no fluorescence reporter gene, was used as the negative-control construct.

Ribozyme-based devices and appropriate controls were inserted into the 3' untranslated region (UTR) of *yEGFP3* in pCS1748 through appropriate restriction endonuclease and ligation-mediated cloning. DNA fragments encoding the ribozyme-based devices and controls were PCR amplified using forward and reverse primers L1-2-fwd (5'-GACCTAGGAAACAAACAAAGCTGTCACC) and L1-2-rev (5'-GGCTCGAGTTTTTATTTTTCTTTTTGCTGTTTCG), respectively, and inserted into pCS1748 via the unique restriction sites AvrII and XhoI, which are located 3 nts downstream of the *yEGFP3* stop codon. Cloned plasmids were transformed into the budding yeast *Saccharomyces cerevisiae* strain W303α (MAT α his3-11, 15 trp1-1 leu2-3 ura3-1 ade2-1) through a standard lithium acetate method (38). All yeast strains

harboring cloned plasmids were maintained on synthetic complete media with a uracil dropout solution containing 2% dextrose (SC-URA) and grown at 30ºC.

The mating fate routing plasmid pCS2293 was constructed by cloning a TEF1 mutant 7 (TEF1m7) promoter (31), and the coding region for Msg5 into the pCS321 backbone (10). The TEF1m7 promoter was PCR amplified from pCS1142 using forward and reverse primers pTEF7-fwd (5'-AAGAGCTCATAGCTTCAAAATGTCTCT ACTCCTTTTT) and pTEF7-rev (5'-AAAGGATCCAACTTAGATTAGATTGCTATGCTTTCTTTCC), respectively, and inserted into pCS321 via the unique restriction sites SacI and BamHI. The *MSG5* gene was PCR amplified from genomic DNA using forward and reverse primers Msg5.K2-fwd (5'-AAAGGATCCAATTAATAGTGCACATGCAATTTCAC) and Msg5-rev (5'-AAAACCTAGGTTAAGGAAGAAACATCATCTG), respectively, and inserted via the unique restriction sites BamHI and AvrII. Ribozyme-based devices and appropriate controls were inserted into the 3' UTR via the unique restriction sites AvrII and XhoI, located immediately downstream of the *MSG5* stop codon as described previously.

The mating reporter construct (pCS1124) was built by cloning FUS1p, a mating-responsive promoter, into the pCS321 backbone (10). The FUS1 promoter was PCR amplified from pDS71 (39) using forward and reverse primers pDS71.Fus1-fwd (5'-TTTGCGGCCGCCCAATCTCAGAGGCTGAGTCT) and pDS71.Fus1-rev (5'-TTTGGATCCTTTGATTTTCAGAAACTTGATGGC), respectively, and inserted upstream of *yEGFP3* in pCS321 via the unique restriction sites NotI and BamHI. The FUS1p-yEGFP3-ADH1t cassette from pCS1124 was cloned into pCS1391, a loxP integrating vector (40), via the unique restriction sites SacI and KpnI to make pCS2292.

FUS1p-yEGFP3-ADH1t was chromosomally integrated into yeast strain EY1119 (W303a Δsst1 Δkss1::HIS3) (41) via homologous recombination using the gene cassette from pCS2292 to construct yeast strain CSY840 (W303a Δsst1 Δkss1::HIS3 trp1::FUS1p-yEGFP3-ADH1t-loxP-KanR). Briefly, the FUS1p-yEGFP3-loxP-KanR cassette was PCR amplified using Expand High Fidelity PCR system (Roche, Indianapolis, IN) from pCS2292 using forward and reverse primers TRP1.INT.all.fwd (5'-GTATACGTGATTAAGCACACAAAGGCAGCTTGGAGTATGTCTGTTATTAATTTCACAGGAAGATTGTACTGAGAGTGCAC) and TRP1.INT.all.rev (5'-TTGCTTTTCAAAAGGCCTGCAGGCAAGTGCACAAACAATACTTAAATAAATACTACTCAGCGACTCACTATAGGGAGACC), respectively, each carrying 60 nts of homologous sequence to the *TRP1* locus. Yeast strain EY1119 was transformed with 12 μg of gel purified PCR product and plated on G418 plates to build yeast strain CSY840. All plasmids and yeast strains constructed in this study are summarized in Supplementary Table S2.1.

2.4.2 Library-scale yeast transformation

Device libraries (Supplementary Figure S2.13) were amplified using forward and reverse primers GAP-L1-2-fwd (5'-TCCATGGTATGGATGAATTGTACAAATAAAGCCTAGGAAACAAACAAAGCTGTCACC) and GAP-L1-2-rev (5'-AAGAAATTCGCTTATTTAGAAGTGGCGCGCCCTCTCGAGTTTTTATTTTTCTTTTTGCTGTTTCG), respectively. The library was inserted into pCS1748 through homologous recombination-mediated gap-repair during

transformation into yeast strain W303 (42). Briefly, an 800 μL library PCR reaction was performed with 160 pmol of each primer and 16 pmol of the library template. 8 μg of the plasmid pCS1748 was digested with AvrII and XhoI. The digested vector was combined with the library PCR product, extracted with phenol chloroform, and precipitated into a dry pellet with ethanol. A Tris-DTT buffer (2.5 M DTT, 1 M Tris, pH 8.0) was added to a 50 mL yeast culture (OD_{600} 1.3-1.5) and incubated at 30ºC for 10-15 min. The yeast were pelleted, washed with chilled Buffer E (10 mM Tris, pH 7.5, 2 mM $MgCl_2$, 270 mM sucrose), and resuspended in Buffer E to a final volume of 300 μL. The yeast mixture was directly added to the precipitated DNA pellet and 50 μL of the mixture was transferred to a chilled 2 mm gap cuvette for electroporation (540 V, 25 μF, 1000 Ω). Following transformation, the cells were resuspended in 1 mL warmed YPD media and incubated at 30ºC for 1 hr. Multiple transformations (~5) were performed to cover the desired library diversity (~10^6-10^7). Transformation efficiencies were determined by plating serial dilutions of the transformants, and transformed cells were propagated in SC-URA media for FACS.

2.4.3 Two-color FACS-based screen

Cells harboring the RNA device libraries and control constructs were washed, resuspended in FACS buffer (1% BSA in PBS), and stained with a DAPI viability dye (Invitrogen). The cell suspension was filtered through a 40 μM cell strainer (BD Systems, San Jose, CA) prior to analysis on a FACSAria II cell sorter (BD Systems). GFP was excited at 488 nm and measured with a splitter of 505 nm and bandpass filter of 525/50 nm. mCherry was excited at 532 nm and measured with a splitter of 600 nm and a

bandpass filter of 610/20 nm. DAPI was excited at 355 nm and measured with a bandpass filter of 450/50 nm. A scatter gate was set based on the forward and side-scatter area of cells harboring the negative-control plasmid (pCS4) to exclude debris, followed by a DAPI-(-) viability gate to exclude dead cells in the DAPI-(+) gate from the analysis. Cells harboring the single-color control plasmids (pCS1585, pCS1749) were analyzed to compensate spillover from GFP to the mCherry detector. A general sorting strategy was followed in which cells harboring devices with targeted activities were analyzed to set a sorting gate on a two-dimensional scatter plot that correlates GFP and mCherry fluorescence. Cells within this gate were collected into SC-URA media and propagated to sufficient density for further screening or analysis.

2.4.4 Ribozyme-based device characterization through flow cytometry analysis

Enriched device libraries from FACS were directly plated onto SC-URA solid medium. Individual colonies were screened and characterized for gene-regulatory activity of the devices based on flow cytometry analysis. The GFP fluorescence was measured on a Quanta flow cytometer (Beckman Coulter, Fullerton, CA). GFP was excited at 488 nm and measured with a splitter of 488 nm and a bandpass filter of 525/40 nm. Cells harboring the negative-control plasmid (pCS4) were analyzed to set the GFP-(-) and GFP-(+) gate. Activities were determined as the geometric mean of the GFP fluorescence based on the GFP-(+) population using FlowJo (Tree Star), and normalized to the geometric mean of the GFP fluorescence of a positive control (sTRSV Contl, a noncleaving sTRSV ribozyme with a scrambled core) that is grown under identical ligand conditions, run in the same experiment, and set to 100%.

Devices that exhibited desired activities were amplified by colony PCR using forward and reverse primers CS653 (5'-GGTCACAAATTGGAATACAACTATAACTCT) and CS654 (5'-CGGAATTAACCCTCACTAAAGGG), respectively, and sequenced. The recovered devices were resynthesized and recloned into the vector backbone to confirm the observed activity. DNA oligos were synthesized and amplified for insertion into pCS1748 using forward and reverse primers L1-2-fwd (5'-GACCTAGGAAACAAACAAAGCTGTCACC) and L1-2-rev (5'- GGCT CGAGTTTTTATTTTTCTTTTTGCTGTTTCG), respectively. The resynthesized devices were inserted into pCS1748 via the unique restriction sites AvrII and XhoI. The reconstructed device plasmids were transformed into the W303 yeast strain through a standard lithium acetate method (38). Cells harboring the selected devices and appropriate controls were prepared as described above for the sorting experiments and analyzed on an LSRII flow cytometer (BD Systems) to characterize the gene-regulatory activity of each device. GFP was excited at 488 nm and measured with a splitter of 505 nm and a bandpass filter of 525/50. mCherry was excited at 532 nm and measured with a splitter of 600 nm LP and a bandpass filter of 610/20 nm. DAPI was excited at 405 nm and measured with a bandpass filter of 450/50 nm. FlowJo was used to process all flow cytometry data. Cells harboring pCS4 and pCS1749 were analyzed to set the mCherry-(-) and mCherry-(+) gates. Activities in the absence or presence of ligand were determined as the geometric mean of the GFP fluorescence based on the mCherry-(+) population, and normalized to the geometric mean of the GFP fluorescence of a positive control (sTRSV Contl, a noncleaving sTRSV ribozyme with a scrambled core) in the absence or presence

of ligand, respectively, to correct for any non-specific effects of ligand on the measured fluorescence (Supplementary Figure S2.8). Reported device activities are the mean and standard deviation of at least three independent experiments.

2.4.5 *In vitro* transcription and purification of ribozyme-based devices

Selected ribozyme-based devices and ribozyme and noncleaving controls were PCR amplified to include an upstream T7 promoter site and spacer sequence and downstream spacer sequence using forward and reverse primers T7-L1-2-fwd (5'-TTCTAATACGACTCACTATAGGGACCTAGGAAACAAACAAAGCTGTCACC) and L1-2-rev (5'-GGCTCGAGTTTTTATTTTTCTTTTTGCTGTTTCG), respectively. A total of 1-2 μg of PCR product was transcribed in a 25 μl reaction, consisting of the following components: 1×RNA Pol Reaction Buffer (New England Biolabs), 2.5 mM rATP, 2.5 mM rCTP, 2.5 mM rUTP, 0.25 mM rGTP, 1 μl RNaseOUT (Invitrogen), 10 mM $MgCl_2$, 1 μl T7 Polymerase (New England Biolabs), and 0.5 μCi α-^{32}P-GTP (MP Biomedicals, Solon, OH). 400 pmol of antisense DNA oligonucleotide, device-blocking (5'-GGTGACAGCTTTGTTTGTTTCCTAGGTCCCCC) and sTRSV-blocking (5'-GCTGTTTCGTCCTCACG), was added to each reaction to inhibit cleavage of the RNA devices and sTRSV hammerhead ribozyme, respectively, during transcription. After incubation at 37°C for 2 hr, NucAway Spin Columns (Ambion, Austin, TX) were used to remove unincorporated nucleotides from the transcription reactions according to manufacturer's instructions. 10 μl aliquots of the recovered RNA were mixed with 3 volumes of RNA stop/load buffer (95% formamide, 30 mM EDTA, 0.25% bromophenol blue, 0.25% xylene cyanol), heated at 95°C for 5 min, snap cooled on ice for 5 min, and

size-fractionated on a denaturing (8.3 M urea) 10% polyacrylamide gel at 25 W for 45 min. Gels were imaged by phosphorimaging analysis on a FX Molecular Imager (Bio-Rad). Uncleaved transcripts were gel extracted and recovered with the ZR Small-RNA™ PAGE Recovery Kit (Zymo Research, Irvine, CA) according to manufacturer's instructions. Samples were stored in sterile, nuclease-free, deionized water at -80°C to limit the extent of RNA self-cleavage prior to performing the cleavage assays.

2.4.6 *In vitro* ribozyme cleavage assays

The purified uncleaved transcripts were incubated in 100 mM NaCl, 50 mM Tris-HCl (pH 7.5) at 95°C for 5 min, cooled at a rate of -1.3°C to 37°C, and held there for 10 min to allow equilibration of secondary structure. A zero time-point aliquot was taken prior to initiating the self-cleavage reaction at 37°C with the addition of $MgCl_2$ to a final concentration of 500 μM. Reactions were quenched at specified time points with addition of 3 volumes of RNA stop/load buffer on ice. Samples were heated 95°C for 5 min, snap cooled on ice for 5 min, and size-fractionated on a denaturing (8.3 M urea) 10% polyacrylamide gel at 25 W for 45 to 60 min. Gels were exposed overnight on a phosphor screen and analyzed for relative levels of the full-length transcript and cleaved products by phosphorimaging analysis. The cleaved product fraction at each time point (F_t) was fit to the single exponential equation $F_t = F_0 + (F_\infty - F_0) \times (1 - e^{-kt})$ using Prism 5 (GraphPad), where F_0 and F_∞ are the fractions cleaved before the start of the reaction and at the reaction endpoint, respectively, and k is the first-order rate constant of self-cleavage. Reported values are the mean of at least three independent experiments.

2.4.7 Measuring mating pathway activity via a transcriptional reporter and halo assays

The mating fate routing plasmids with ribozyme-based devices and appropriate controls were transformed into yeast strain CSY840. Cells were inoculated into the appropriate drop-out media, grown overnight at 30°C, and back diluted into fresh media in the presence or absence of 5 mM theophylline to an OD_{600} of <0.1. After growing for 3 hr at 30°C, cells were stimulated with saturating pheromone levels, to a final concentration of 100 nM α mating factor acetate salt (Sigma-Aldrich, St. Louis, MO), to activate the mating pathway. After 3 hr of stimulation, GFP fluorescence levels from the pFus1-yEGFP3 reporter were evaluated via flow cytometry using a Cell Lab Quanta SC flow cytometer (Beckman Coulter, Fullerton, CA). Normalized pathway activity is calculated as the geometric mean of three biological replicates of each sample normalized to the blank plasmid control (no *MSG5*) in the absence of theophylline. Mating associated cell-cycle arrest was evaluated via halo assays (43). Halo assays were performed on cultures grown overnight, back diluted into fresh media in the absence of theophylline, and grown another 6 hr. 200 μl of each replicate was plated on the appropriate drop-out plates in the absence or presence of 5 mM theophylline. A gradient of α mating factor was established by saturating a filter disk (2 mm diameter) of Whatman paper with 9 μl of 0.1 mg/mL α mating factor and placing the disk on the center of the plate. Cells were grown for 18 hr at 30°C and imaged via epi-white illumination with a GelDoc XR+ System (Bio-Rad). To control for any possible differences in growth rate between replicates, plates are compared within one biological replicate ensuring differences in

growth rate arise from divergence following plating in the absence or presence of theophylline.

2.5 Supplementary Information

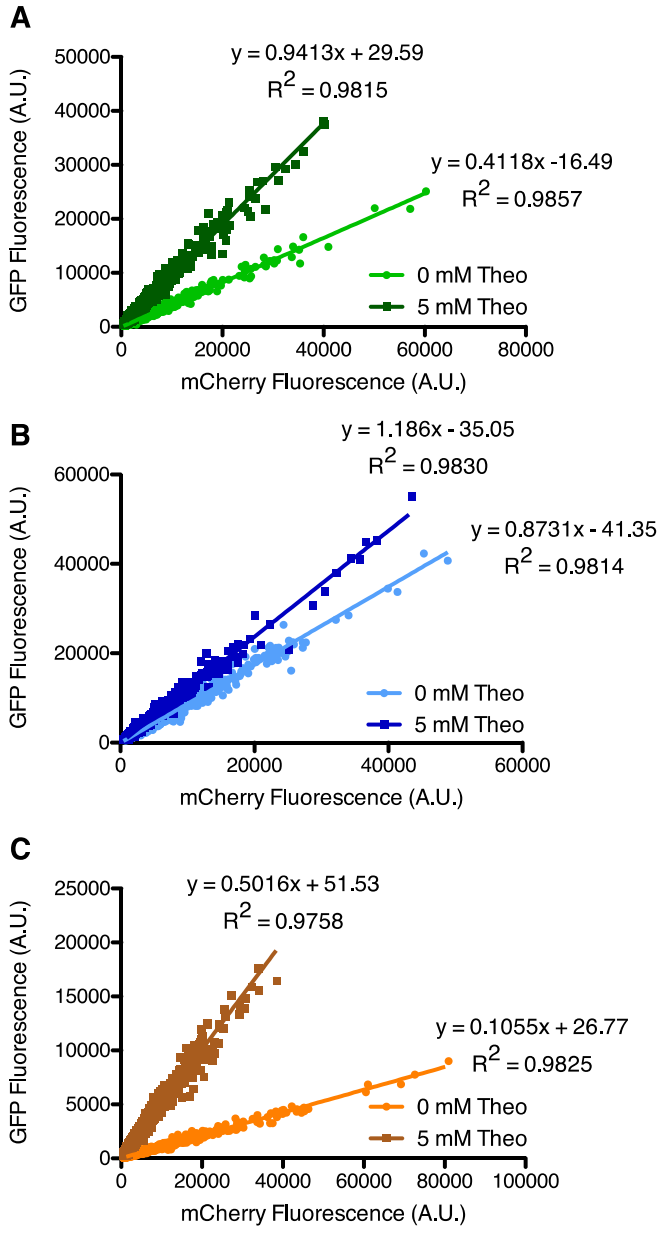

Supplementary Figure S2.1 Linear correlation between mCherry and GFP fluorescence for L2b1 (A), L2b5 (B), and L2b8 (C) devices within the two-color construct. For each device, 2,000 cells are plotted from a single representative experiment at 0 and 5 mM theophylline (theo). Linear regression and R^2 values are reported and support a distinct slope for different device regulatory activities.

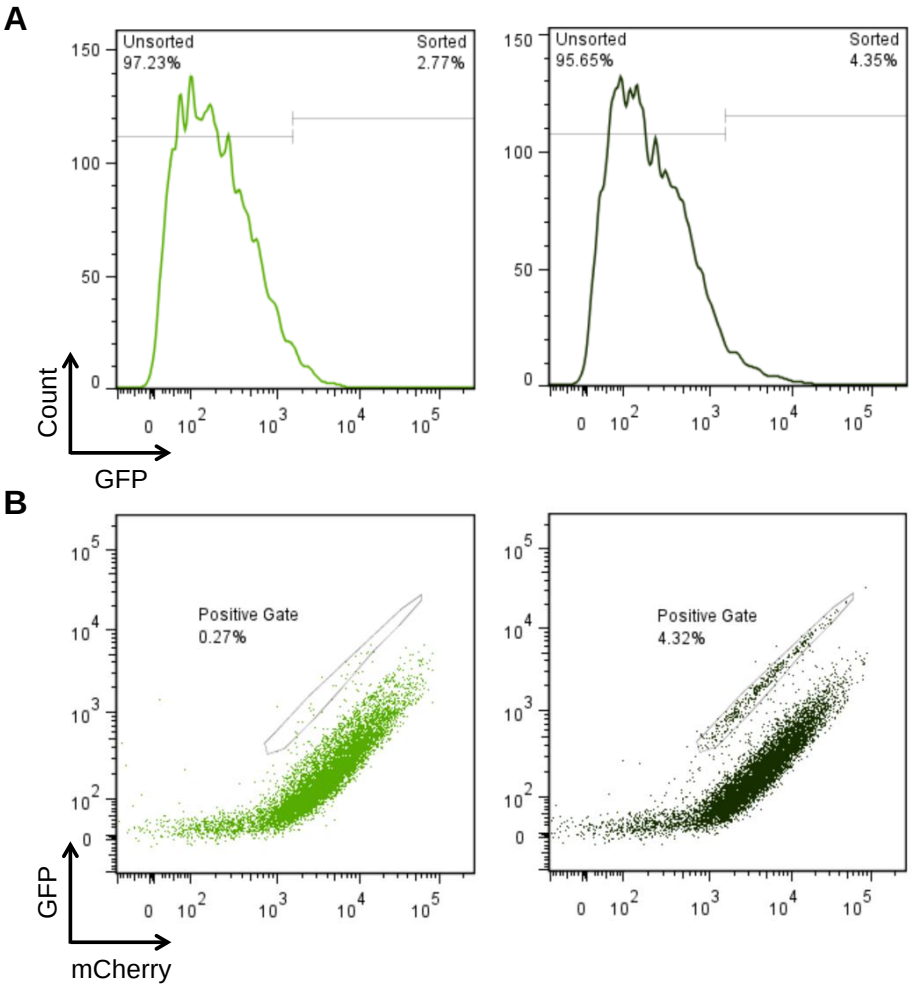

Supplementary Figure S2.2 Comparison of resolution between single-color and two-color screens. Enriched sN10 library after one sorting cycle and an additional negative sort was analyzed through flow cytometry in the presence and absence of 5 mM theophylline. The positive sorting gate is set by the activity of the parent device in the presence of 5 mM theophylline. In the absence of theophylline, the gate contains cells that are false positives; in the presence of theophylline, the gate contains both true and false positives. (A) The left GFP histogram represents the enriched library in the absence of theophylline, while the right GFP histogram represents the enriched library in the presence of theophylline. For the single-color screen, a hypothetical sorting gate was set based on the percentage of cells isolated from the corresponding two-color screen (4.32%). If a single-color screen were performed, ~64% (2.77/4.35) of the isolated cells would be false positives. (B) The left two-color scatter plot represents the enriched library in the absence of theophylline, while the right two-color scatter plot represents the enriched library in the presence of theophylline. The two-color screen exhibits high resolving power, such that only ~6% (0.27/4.32) of the isolated cells were false positives,

resulting in a significant improvement in enrichment efficiency over the single-color screen.

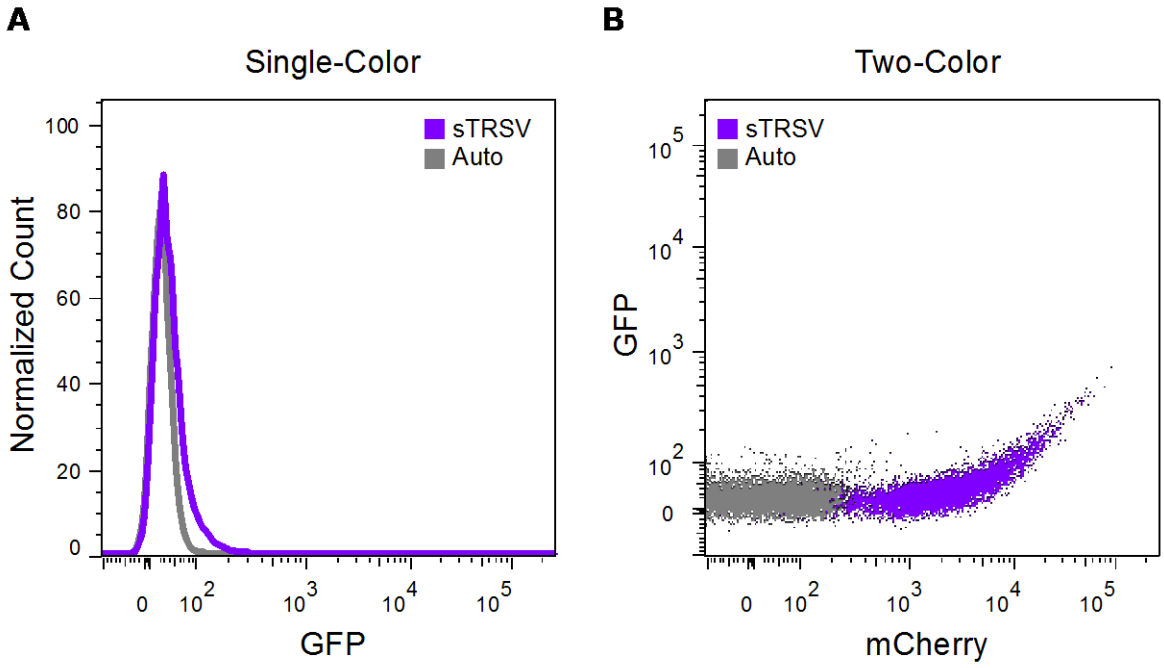

Supplementary Figure S2.3 The two-color sorting strategy supports separation of autofluorescent and low expression cell populations. sTRSV (the active ribozyme control) exhibits ~1.2% normalized GFP fluorescence, relative to a noncleaving ribozyme positive control (sTRSV Contl) with a scrambled core. (A) A cell population harboring the sTRSV construct exhibits low fluorescence levels that overlap significantly with a cell population harboring no fluorescence reporter gene in the single-color histogram. (B) The sTRSV and autofluorescent populations separate based on mCherry expression in the two-color plot, allowing cells exhibiting low GFP expression due to stringent device gene-regulatory activity to be effectively enriched through two-color sorting.

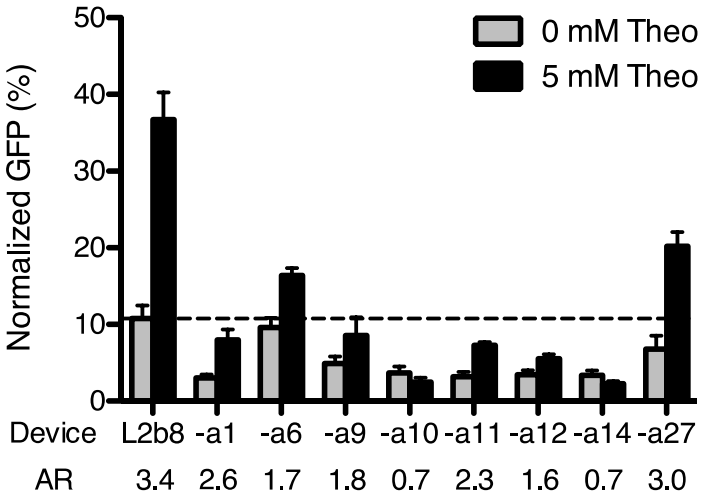

Supplementary Figure S2.4 An actuator sort preserves switching activity in 6 out of 8 characterized devices. Basal activity of the parent device, L2b8, is indicated by a dashed line. Gene-regulatory activities are reported as the geometric mean of the GFP fluorescence of the indicated sample normalized to that of a positive control (sTRSV Contl, a noncleaving sTRSV ribozyme with a scrambled core) that is grown under identical ligand conditions and is set to 100%. Reported values are the mean and standard deviation of at least three independent experiments. The activation ratio (AR), determined as the ratio of gene expression levels in the presence and absence of theophylline (theo), is indicated for each device.

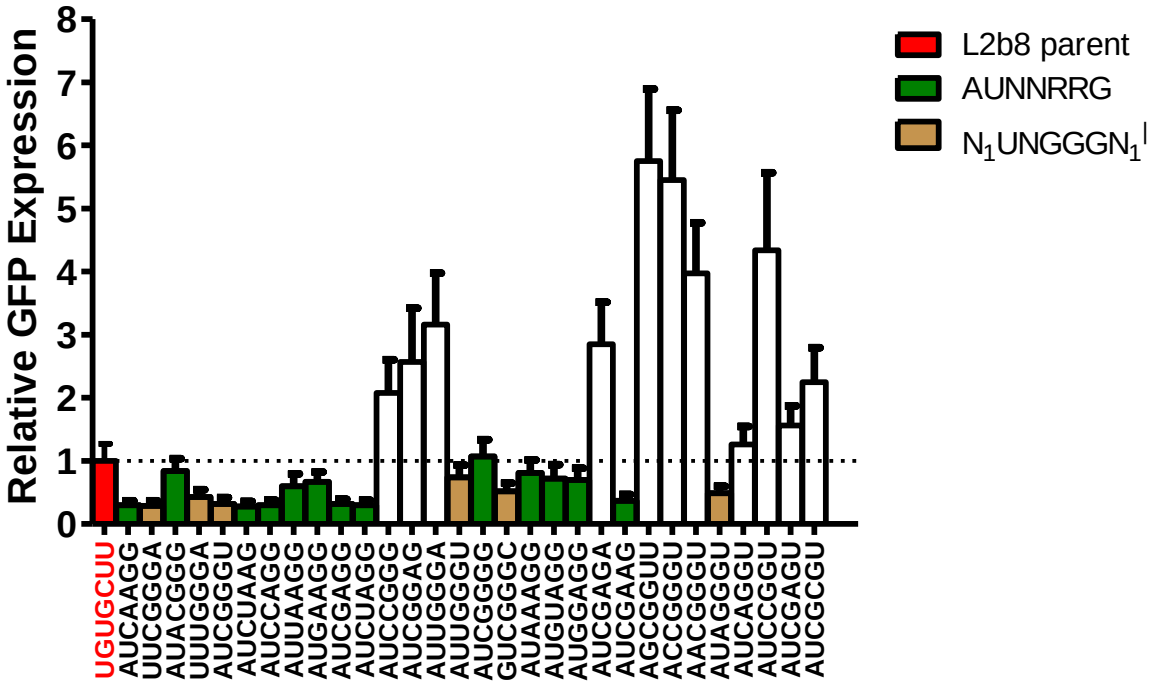

Supplementary Figure S2.5 Point mutation analyses of variant loop I sequences identify consensus sequences of ribozyme variants supporting improved gene-regulatory activities. The impact of point mutations to the recovered loop I sequences on basal activity was measured by flow cytometry. Relative expression levels are reported as the geometric mean of the GFP fluorescence of the indicated sample normalized to that of the L2b8 parent device. Reported values are the mean and standard deviation of at least three independent experiments. Two putative loop I consensus sequences were supported from the sequences recovered from the actuator library screen: a heptaloop (AUYNRRG) and a triloop (NUYGGGN$^{|}$).

Analysis of the point mutants made to interrogate nucleotide base constraints at each position of the heptaloop sequence found that any base (N) is tolerable at the third and fourth positions, but specific identities at the third position result in improved basal activity (C > A/U > G). The fifth and sixth positions accept both purine bases (A, G) and retain activity similar to that of the L2b8 parent; however, an adenine base (A) in the fifth position results in improved basal activity. Point mutants verified the requirement of a guanine base (G) in the seventh position.

For the triloop sequence, point mutants indicate that any combination of bases in the first and seventh positions resulting in canonical Watson-Crick base pairing (AU, GC; order independent) results in improved basal activity. The bases in the second and sixth positions must result in a Watson-Crick GU wobble pair, where this requirement is sensitive to identity and order (i.e., standard Watson-Crick pairing abolishes improved

activity). The point mutants indicate that the third position is able to accept any nucleotide base (N), whereas a guanine base (G) is required at the fourth and fifth positions to retain improved activity relative to the L2b8 parent device.

A L2b1:

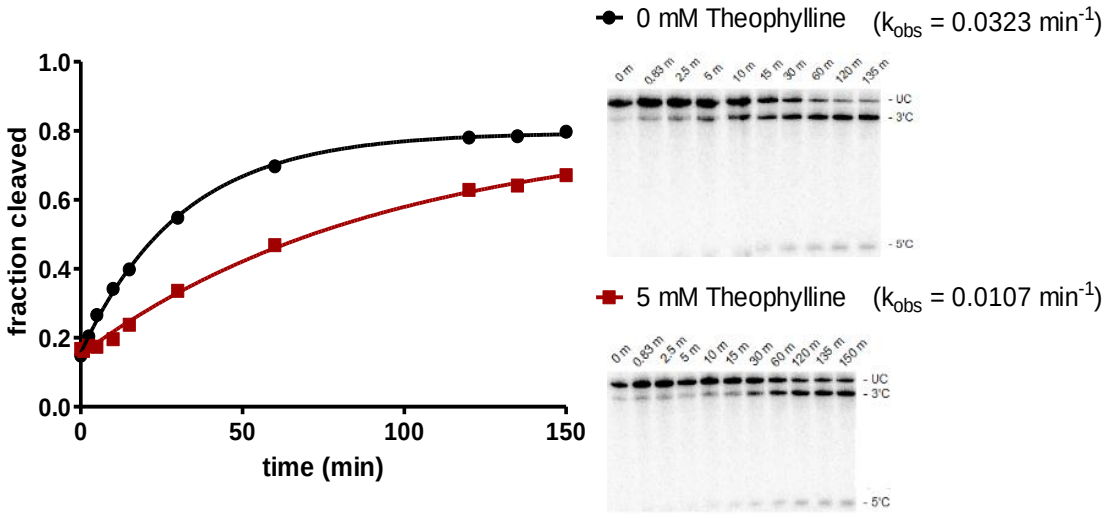

B L2b5:

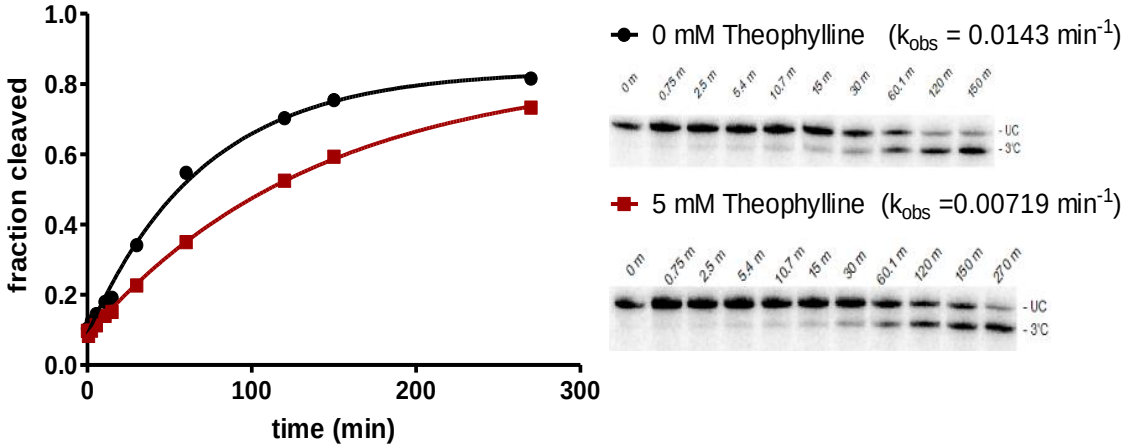

C L2b8:

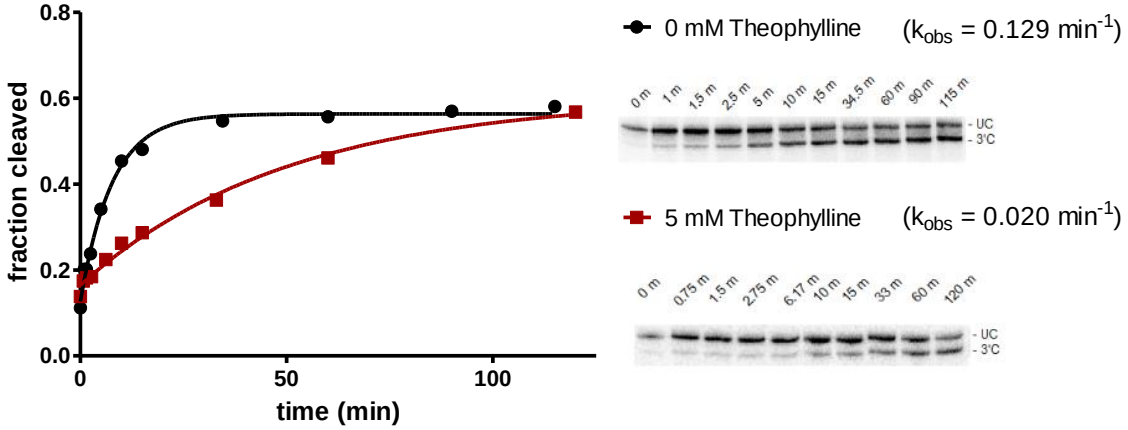

D L2b8-a1:

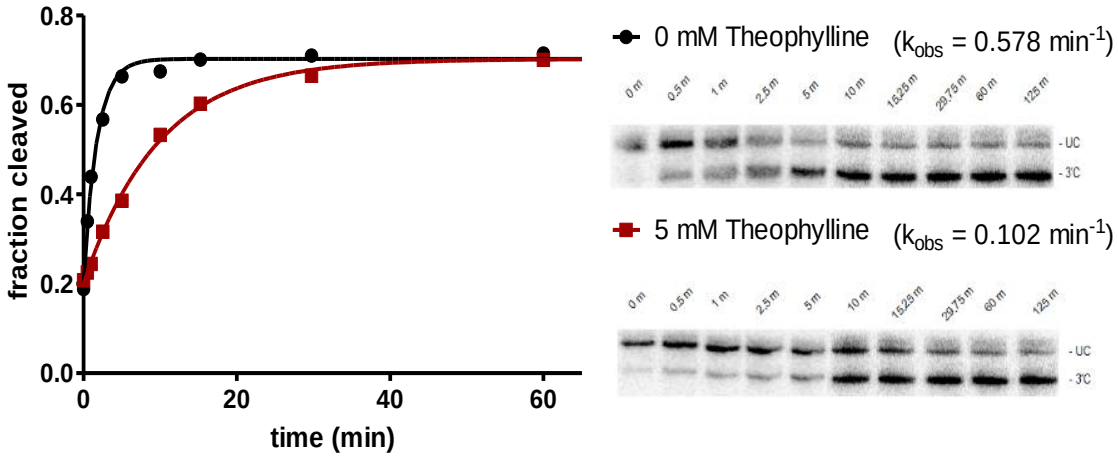

E L2b8-a14:

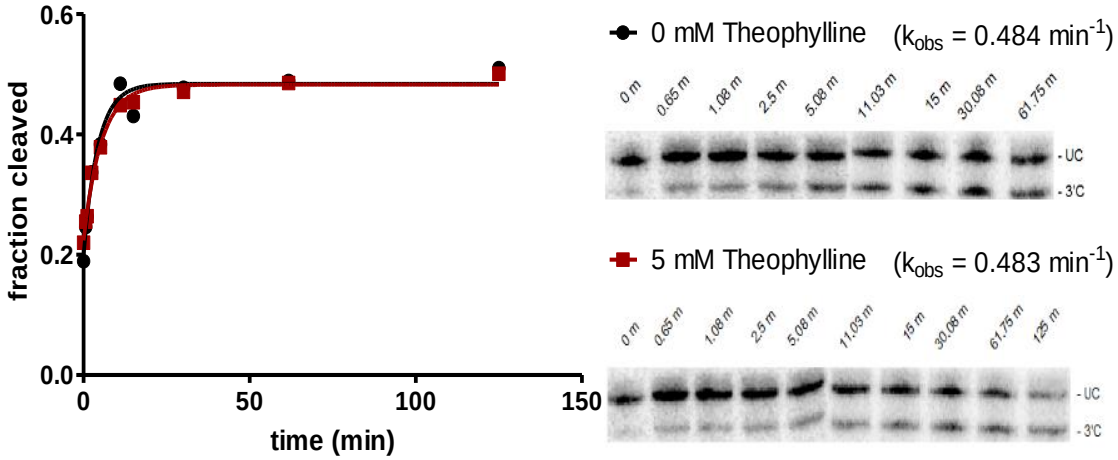

F L2b8-a1-t41:

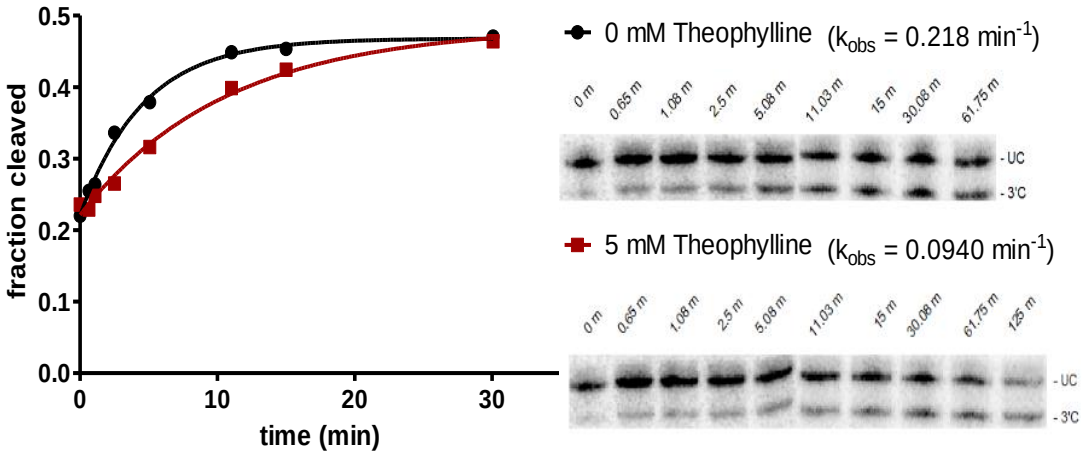

G sTRSV ribozyme:

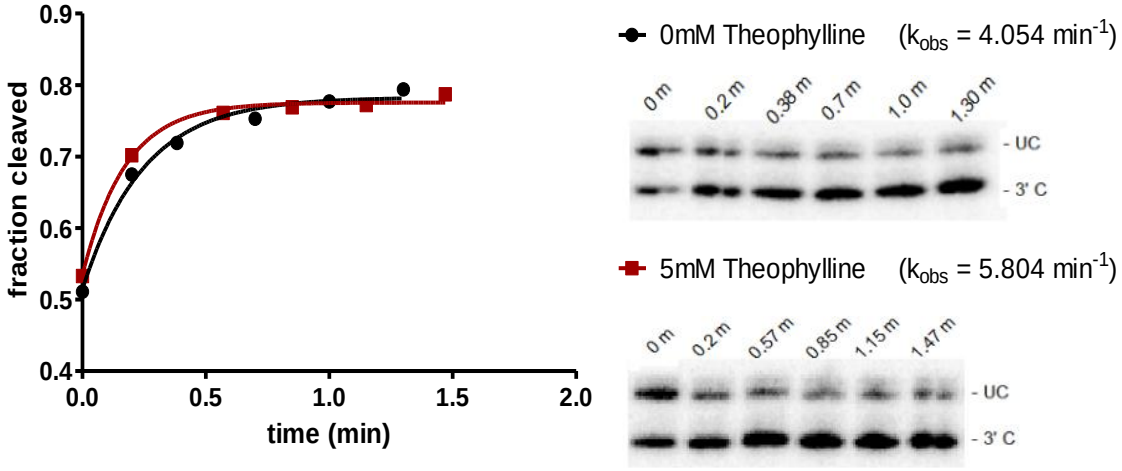

H

RNA Device	Cleavage Rate (*k*, min^{-1})	
	0 mM theophylline	**5 mM theophylline**
L2b1	0.033 ± 0.008	0.011 ± 0.003
L2b5	0.013 ± 0.002	0.007 ± 0.001
L2b8	0.14 ± 0.02	0.025 ± 0.009
L2b8-a1	0.7 ± 0.3	0.1 ± 0.03
L2b8-a14	0.9 ± 0.4	1.0 ± 0.2
L2b8-a1-t41	0.16 ± 0.05	0.096 ± 0.02
sTRSV ribozyme	4.3 ± 0.8	4.3 ± 1.4

Supplementary Figure S2.6 Representative cleavage assays for measuring cleavage rate constants (*k*) for ribozyme-based devices and controls. A representative assay is shown for each device in the absence and presence (0 and 5 mM, respectively) of theophylline: L2b1 (A), L2b5 (B), L2b8 (C), L2b8-a1 (D), L2b8-a14 (E), L2b8-a1-t41 (F), and sTRSV ribozyme (G). Bands for both the cleaved products (5'C, 3'C) and the full-length uncleaved substrate (UC) are shown for L2b1. For subsequent devices, the shorter 5'C product is omitted from the inset image for clarity. Methods used to prepare full-length, uncleaved RNA transcripts and conditions of the cleavage assays are detailed in the Materials and Methods section of the main text. Briefly, RNA was heated to 95°C for 5 min and cooled to 37°C in a secondary structure refolding buffer (100 mM NaCl, 50 mM Tris-HCl (pH 7.5)). A zero time point aliquot was removed prior to initiating the reaction with addition of $MgCl_2$ to a final concentration of 500 μM. Reactions were quenched at the indicated time points. At least seven time points were taken in each cleavage assay to capture the cleavage dynamics of RNA devices exhibiting different cleavage kinetics. Phosphorimaging analysis of relative levels of the UC, 5'C, and 3'C bands was used to determine the fraction cleaved at each time point (F_t). The fraction cleaved at the beginning (F_0) and end of reaction (F_∞) varied between assays, but all assays were well-fit to the single exponential equation ($R^2 > 0.95$):

$$F_t = F_0 + (F_\infty - F_0) \times (1 - e^{-kt})$$

The black and red fit lines represent assays performed at 0 and 5 mM theophylline, respectively. The cleavage rate constant value (*k*) was determined for each assay. The reported *k* for each device and theophylline assay condition is the mean and standard deviation of at least three independent experiments (H).

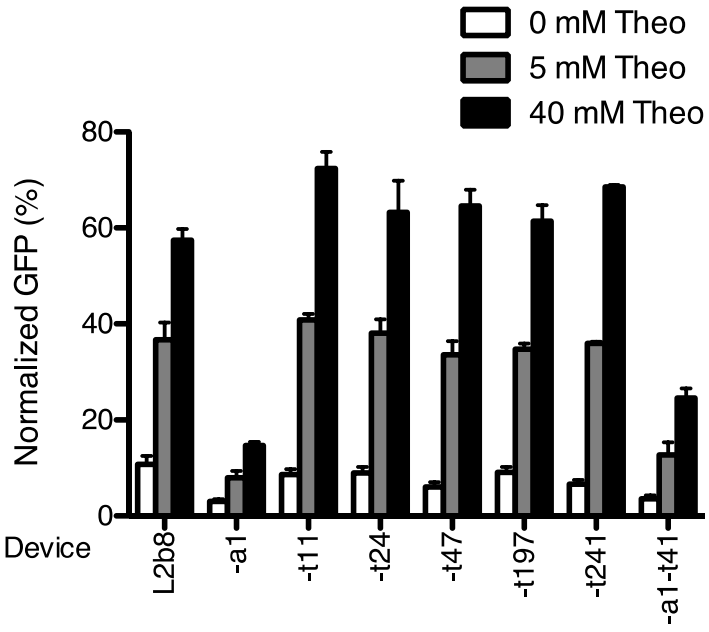

AR at 5 mM Theophylline	3.4	2.6	4.7	4.2	5.5	3.8	5.4	3.6
AR at 40 mM Theophylline	5.3	4.8	8.4	7.0	10.7	6.8	10.4	6.9

Supplementary Figure S2.7 Increased input ligand concentration results in higher device ON states. Increasing ligand concentration to 40 mM theophylline (theo) increases device activation ratio (AR) compared to 5 mM theophylline. Gene-regulatory activities are reported as the geometric mean of the GFP fluorescence of the indicated sample normalized to that of a positive control (sTRSV Contl, a noncleaving sTRSV ribozyme with a scrambled core) that is grown under identical ligand conditions and is set to 100%. Reported values are the mean and standard deviation of at least three independent experiments. The activation ratio (AR), determined as the ratio of gene expression levels in the presence and absence of theophylline (theo), is indicated for each device.

A

	GFP (A.U.)			mCherry (A.U.)			Viability (%)		
	0mM Theo	**5mM Theo**	**Ratio**	**0mM Theo**	**5mM Theo**	**Ratio**	**0mM Theo**	**5mM Theo**	**Ratio**
Replicate 1	3969.31	4532.12	1.14	2097.92	2339.26	1.12	98.24	97.16	0.99
Replicate 2	6282.93	6868.85	1.09	2699.57	2589.77	0.96	97.51	96.60	0.99
Replicate 3	2960.27	3129.06	1.06	2505.69	2496.95	1.00	96.47	96.73	1.00
Mean ± S.D.			1.10 ± 0.04			1.02 ± 0.08	97.41 ± 0.89	96.83 ± 0.29	0.99 ± 0.01
	0mM Theo	**40mM Theo**	**Ratio**	**0mM Theo**	**40mM Theo**	**Ratio**	**0mM Theo**	**40mM Theo**	**Ratio**
Replicate 1	4687.84	6380.01	1.36	5653.65	5504.26	0.97	97.63	96.62	0.99
Replicate 2	4777.71	6249.37	1.31	5137.39	5502.14	1.07	98.39	96.59	0.98
Replicate 3	4878.88	5977.69	1.23	4722.92	4921.71	1.04	97.99	94.83	0.97
Mean ± S.D.			1.30 ± 0.07			1.03 ± 0.05	98.00 ± 0.38	96.01 ± 1.02	0.98 ± 0.01
	0mM Tc	**1mM Tc**	**Ratio**	**0mM Tc**	**1mM Tc**	**Ratio**	**0mM Tc**	**1mM Tc**	**Ratio**
Replicate 1	2585.21	2382.28	0.92	2791.13	2278.18	0.82	98.05	98.72	1.01
Replicate 2	2310.21	2036.61	0.88	2896.15	2628.35	0.91	97.73	98.74	1.01
Replicate 3	2326.70	2203.89	0.95	3694.26	3691.82	1.00	97.75	98.22	1.00
Mean ± S.D.			0.92 ± 0.03			0.91 ± 0.09	97.84 ± 0.18	98.56 ± 0.29	1.01 ± 0.00

B

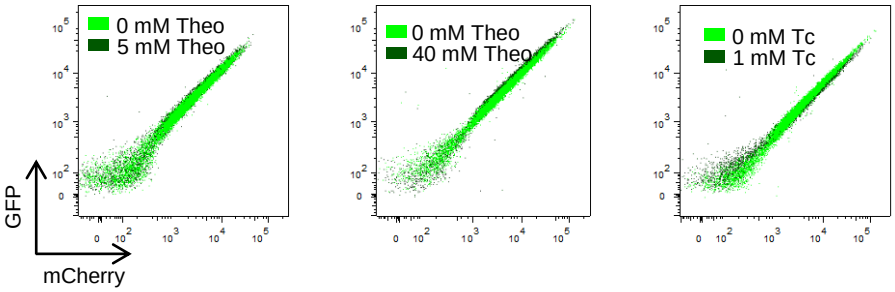

Supplementary Figure S2.8 Quantification of nonspecific ligand effect on fluorescence intensity and cell viability. (A) Unnormalized data for GFP fluorescence, mCherry fluorescence, and cell viability for the positive control construct (sTRSV Contl, a noncleaving sTRSV ribozyme with a scrambled core) in all ligand conditions tested. Fluorescence values are reported as the geometric mean of the GFP or mCherry fluorescence of sTRSV Contl. Cell viability is reported as the percentage of cells included in the DAPI-(-) gate. Mean and standard deviation of three independent experiments are indicated. The ratio of fluorescence levels or cell viability percentages in the presence and absence of theophylline (theo) or tetracycline (tc) is indicated for each ligand condition. Variability in absolute GFP or mCherry signal among replicates for an individual ligand condition is due to differences in instrument calibration between experiments. Values for each replicate pair in the absence and presence of ligand were obtained in the same experiment with identical instrument calibration. (B) Scatter plots for sTRSV Contl under each ligand condition from a single representative experiment.

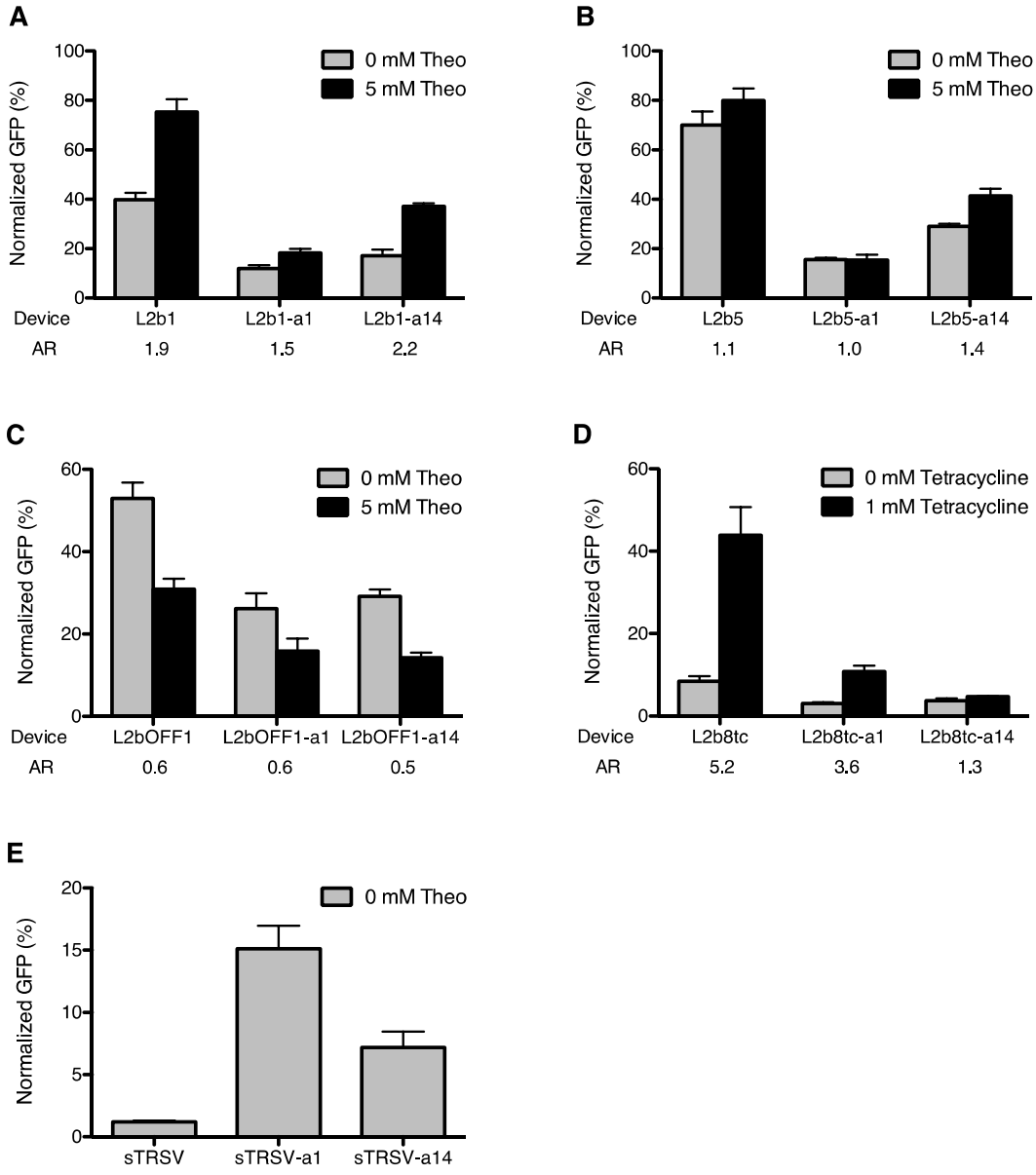

Supplementary Figure S2.9 Component swapping demonstrates modularity of the optimized actuator components. Replacement of the loop I sequence with the a1 or a14 sequence decreases basal activity in all devices tested, including theophylline (theo)-responsive ON (A, B) and OFF (C) switches and a tetracycline-responsive ON switch (D). Switching activity is maintained in most devices. Notably, replacement of the loop I sequence in the sTRSV ribozyme (E) significantly increases basal activity. Gene-regulatory activities are reported as the geometric mean of the GFP fluorescence of the indicated sample normalized to that of a positive control (sTRSV Contl, a noncleaving sTRSV ribozyme with a scrambled core) that is grown under identical ligand conditions and is set to 100%. Reported values are the mean and standard deviation of at least three

independent experiments. The activation ratio (AR), determined as the ratio of gene expression levels in the presence and absence of theophylline (theo) (A, B, C) or of tetracycline (D), is indicated for each device.

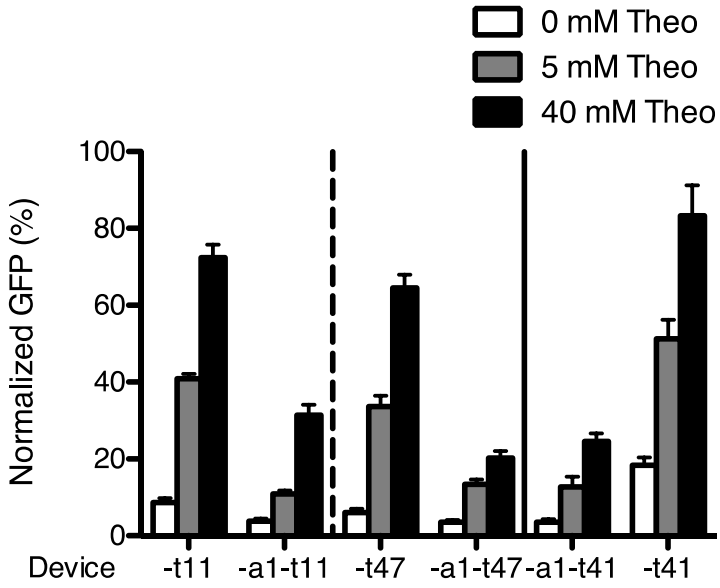

Device	-t11	-a1-t11	-t47	-a1-t47	-a1-t41	-t41
AR at 5 mM Theophylline	4.7	2.8	5.5	3.8	3.6	2.8
AR at 40 mM Theophylline	8.4	8.2	10.7	5.7	6.9	4.5

Supplementary Figure S2.10 The activities of the optimized actuator components are maintained in the context of the newly selected transmitter components. For devices isolated from the tN11 sort (L2b8-t11 and L2b8-t47), replacement of the actuator loop I sequence with the a1 sequence results in lower basal activity. For L2b8-a1-t41, which was isolated from the a1-tN11 sort, replacement of the a1 sequence with the loop I sequence of L2b8 results in higher basal activity. Gene-regulatory activities are reported as the geometric mean of the GFP fluorescence of the indicated sample normalized to that of a positive control (sTRSV Contl, a noncleaving sTRSV ribozyme with a scrambled core) that is grown under identical ligand conditions and is set to 100%. Reported values are the mean and standard deviation of at least three independent experiments. The activation ratio (AR), determined as the ratio of gene expression levels in the presence and absence of theophylline (theo), is indicated for each device.

A L2b8 parent (Loop I: UGUGCUU)

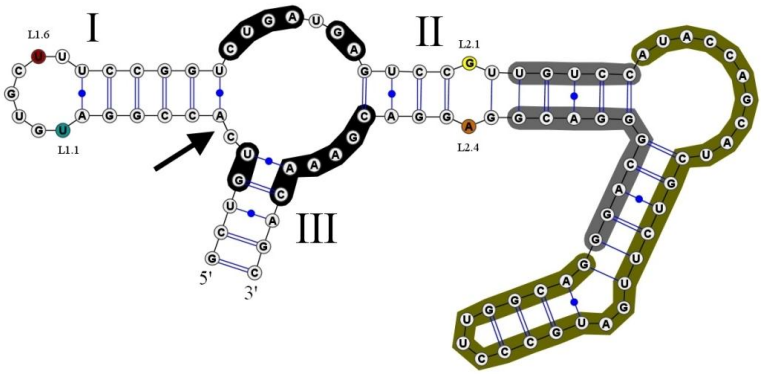

B aN7 heptaloop consensus (AUCNARG)

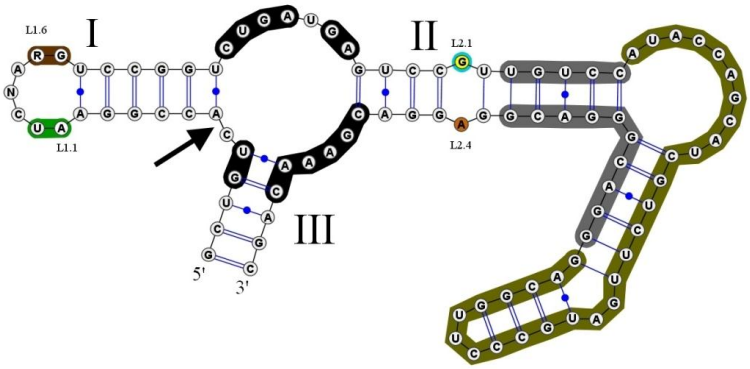

C Newt hammerhead ribozyme

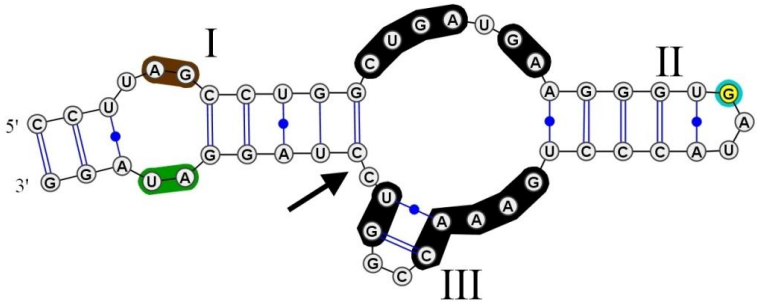

D aN7 triloop consensus ($N_1UN_2GGGN_1$)

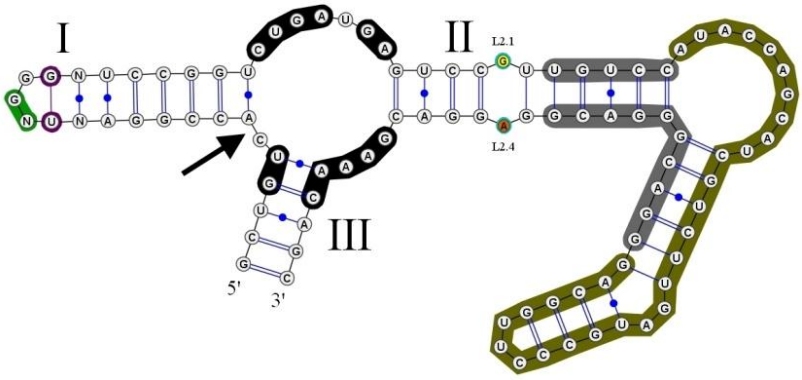

E CarSVRNA(-) hammerhead ribozyme

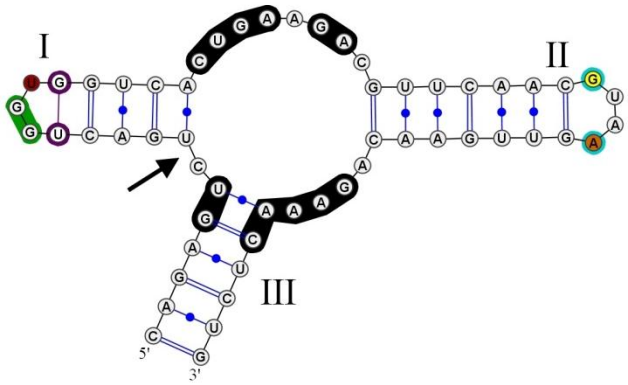

Supplementary Figure S2.11 Secondary structure analysis indicates similarities between engineered RNA devices and natural hammerhead ribozymes (HHRzs). The HHRz invariant nucleotide bases are boxed in black, and the cleavage site is denoted by an arrow in all structures. In RNA device structures (A, B, D), nucleotide bases of the transmitter and aptamer domains are boxed in grey and olive green respectively. Using the common numbering system for HHRz with apical loops (44), nucleotide bases highlighted in cyan (L1.1 U) and red (L1.6 U) are those conforming to the common HHRz loop I motif, UN_mYN, where m is typically 3 or 4 bases. Common loop II motif nucleotide bases, (RN_nA), are highlighted in yellow (L2.1 G) and orange (L2.1 A), where n is usually 2 or 4 bases (27). R and Y denote purine and pyrimidine bases respectively. (A) The HHRz core of the L2b8 parent device forms a predicted GU base pair at L2.2-L2.3 due to transmitter-sensor integration into loop II when analyzed by RNAstructure folding software (45). HHRz loop sequence similarities exist between a device containing the variant heptaloop consensus sequence selected in this study (B) and the newt HHRz (C). In loop I, both HHRz structures have AU in the first two positions 5’ from the

catalytic core (boxed in green) and RG in last two positions (boxed in brown). In loop II, both structures have a G nucleotide not constrained in a Watson-Crick base pair (circled in cyan). Loop sequence similarities also exist between a device containing the variant triloop consensus sequence (D) and the CarSVRNA(-) HHRz (E). Both loop I sequences in these HHRzs contain a triloop with a GU base pair closing the loop (circled in purple) and accommodate GG in the first two positions 5’ from the catalytic core (boxed in green). In loop II, both HHRz structures have L2.1 G and L2.4 A nucleotides not constrained in Watson-Crick base pairs, available for loop I-loop II interaction, circled in cyan (27). Secondary structures rendered using VARNA software (46).

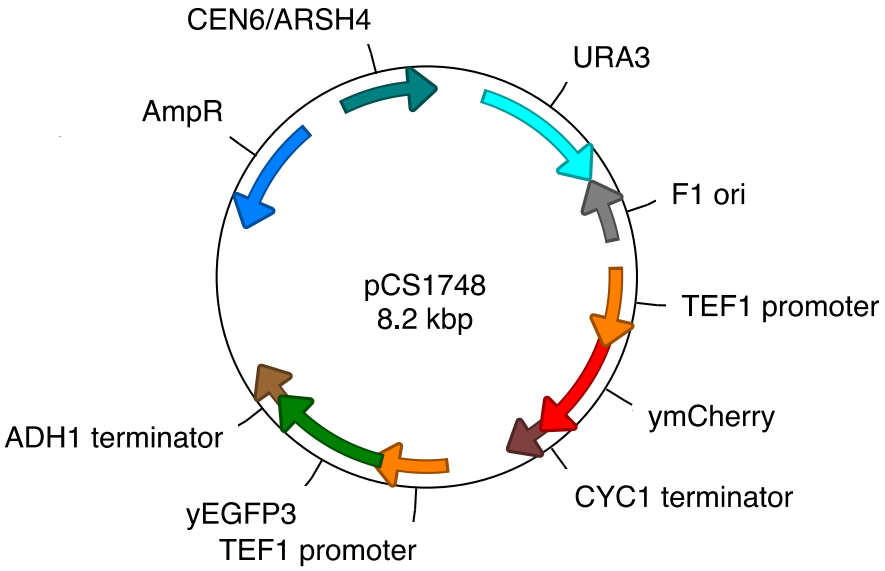

Supplementary Figure S2.12 Plasmid map of pCS1748. RNA devices are inserted in the 3' UTR of yEGFP3.

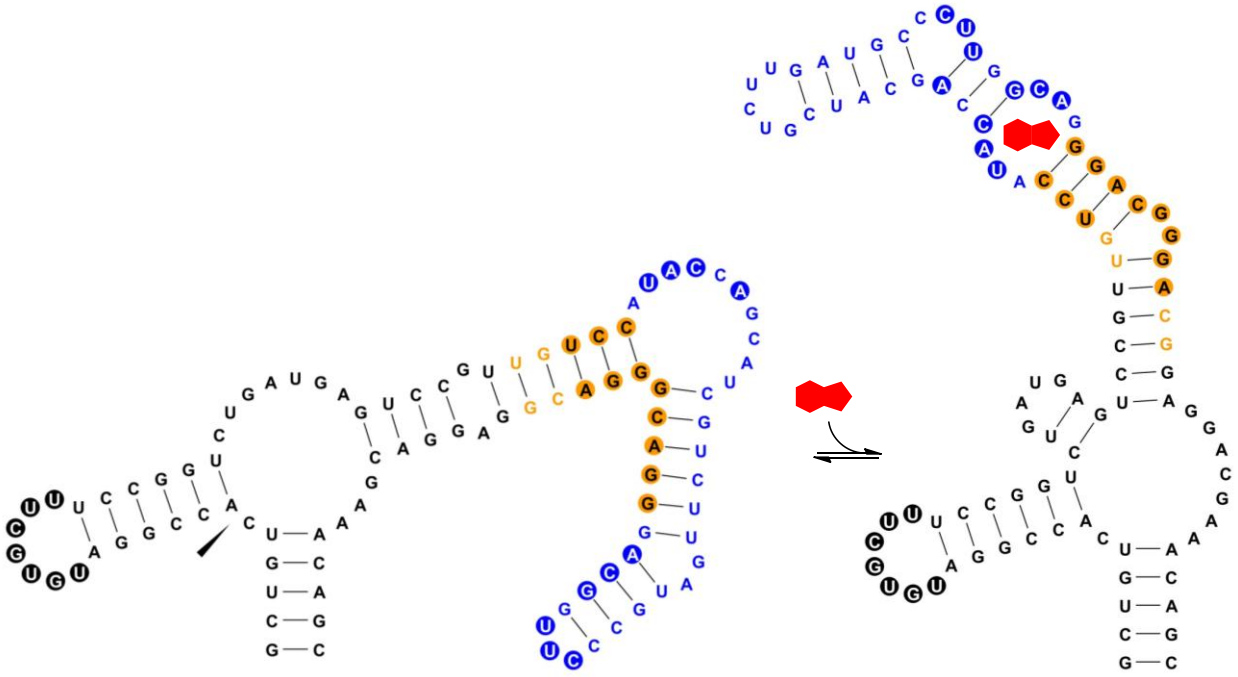

Supplementary Figure S2.13 Library design for sN10 sensor, aN7 actuator, and tN11 and a1-tN11 transmitter libraries. Predicted secondary structures of the active ribozyme conformation with unbound theophylline aptamer (left) and the inactive ribozyme conformation with bound theophylline aptamer (right) are shown. The sequence for the L2b8 parent device is shown. Nucleotides that comprise the sensor, actuator, and transmitter components are colored blue, black, and yellow, respectively. Theophylline is represented by the red polygon. Filled circles within each component indicate nucleotides randomized to generate respective device libraries. Secondary structures were predicted by RNAstructure folding software (45) and rendered using VARNA software (46).

Supplementary Table S2.1 Summary of plasmids and yeast strains constructed.

Plasmid	Color Controls
pCS1748	two-color screening plasmid: TEF1p-GFP-ADH1t and TEF1p-mCherry-CYC1t
pCS1585	single-color plasmid: TEF1p-GFP-ADH1t
pCS1749	single-color plasmid: TEF1p-mCherry-CYC1t
	Ribozyme-based Devices and Controls
pCS1750	pCS1748+sTRSV
pCS1751	pCS1748+sTRSV Contl
pCS1752	pCS1748+L2b1
pCS1753	pCS1748+L2b8
pCS2260	pCS1748+L2b5
pCS2261	pCS1748+L2b8-a1
pCS2262	pCS1748+L2b8-a6
pCS2263	pCS1748+L2b8-a9
pCS2264	pCS1748+L2b8-a10
pCS2265	pCS1748+L2b8-a11
pCS2266	pCS1748+L2b8-a12
pCS2267	pCS1748+L2b8-a14
pCS2268	pCS1748+L2b8-a27
pCS2269	pCS1748+L2b8-t11
pCS2270	pCS1748+L2b8-t24
pCS2271	pCS1748+L2b8-t47
pCS2272	pCS1748+L2b8-t197
pCS2273	pCS1748+L2b8-t241
pCS2274	pCS1748+L2b8-a1-t41
pCS2275	pCS1748+L2b8-a1-t55
pCS2276	pCS1748+L2b8-a1-t64
pCS2277	pCS1748+L2b1-a1
pCS2278	pCS1748+L2b1-a14
pCS2279	pCS1748+L2b5-a1
pCS2280	pCS1748+L2b5-a14
pCS2281	pCS1748+L2bOFF1
pCS2282	pCS1748+L2bOFF1-a1
pCS2283	pCS1748+L2bOFF1-a14
pCS2284	pCS1748+L2b8tc
pCS2285	pCS1748+L2b8tc-a1
pCS2286	pCS1748+L2b8tc-a14

pCS2287	pCS1748+sTRSV-a1
pCS2288	pCS1748+sTRSV-a14
pCS2289	pCS1748+L2b8-a1-t11
pCS2290	pCS1748+L2b8-a1-t47
pCS2291	pCS1748+L2b8-t41
	Yeast Mating Pathway
pCS1124	FUS1p-GFP-ADH1t
pCS2292	FUS1p-GFP-ADH1t in LoxP integrating vector
pCS2293	TEF1m7p-Msg5-ADH1t
pCS2294	pCS2293+sTRSV
pCS2295	pCS2293+L2b8-a1
pCS2297	pCS2293+L2b8
pCS2299	pCS2293+sTRSV Contl
Strain	
CSY840	W303a Δsst1 Δkss1::HIS3 trp1::FUS1p-yEGFP3-ADH1t-loxP-KanR

Acknowledgements

We thank C Crumpton and M Bigos of the Stanford Shared FACS facility. This work was supported by the National Institutes of Health (R01GM086663), the National Science Foundation (CBET-0917638, CCF-0943269), the Defense Advanced Research Projects Agency (HR0011-11-2-0002), the National Sciences and Engineering Research Council of Canada (fellowship to ABK), and the Alfred P. Sloan Foundation (fellowship to CDS).

Contributions

JCL designed and performed research and wrote the paper; ALC designed and performed research associated with the two-color FACS-based screen and wrote the paper; ABK designed and performed research associated with the *in vitro* characterization of ribozyme cleavage rates and wrote the paper; KEG designed and performed research associated with the MAPK pathway and wrote the paper; CDS designed research and wrote the paper.

References

1. Chen, Y.Y., Jensen, M.C. and Smolke, C.D. (2010) Genetic control of mammalian T-cell proliferation with synthetic RNA regulatory systems. *Proc Natl Acad Sci U S A*, **107**, 8531-8536.
2. Culler, S.J., Hoff, K.G. and Smolke, C.D. (2010) Reprogramming cellular behavior with RNA controllers responsive to endogenous proteins. *Science*, **330**, 1251-1255.
3. Ro, D.-K., Paradise, E.M., Ouellet, M., Fisher, K.J., Newman, K.L., Ndungu, J.M., Ho, K.A., Eachus, R.A., Ham, T.S., Kirby, J. *et al.* (2006) Production of the antimalarial drug precursor artemisinic acid in engineered yeast. *Nature*, **440**, 940-943.
4. Sinha, J., Reyes, S.J. and Gallivan, J.P. (2010) Reprogramming bacteria to seek and destroy an herbicide. *Nat Chem Biol*, **6**, 464-470.
5. Joyce, G.F. (2007) Forty years of in vitro evolution. *Angew Chem Int Ed Engl*, **46**, 6420-6436.
6. Seeman, N.C. (2005) From genes to machines: DNA nanomechanical devices. *Trends Biochem Sci*, **30**, 119-125.
7. Win, M.N., Liang, J.C. and Smolke, C.D. (2009) Frameworks for programming biological function through RNA parts and devices. *Chem Biol*, **16**, 298-310.
8. Fedor, M.J. and Williamson, J.R. (2005) The catalytic diversity of RNAs. *Nat Rev Mol Cell Biol*, **6**, 399-412.
9. Bartel, D.P. (2009) MicroRNAs: target recognition and regulatory functions. *Cell*, **136**, 215-233.

10. Win, M.N. and Smolke, C.D. (2007) A modular and extensible RNA-based gene-regulatory platform for engineering cellular function. *Proceedings of the National Academy of Sciences*, **104**, 14283-14288.

11. Link, K.H., Guo, L., Ames, T.D., Yen, L., Mulligan, R.C. and Breaker, R.R. (2007) Engineering high-speed allosteric hammerhead ribozymes. *Biol Chem*, **388**, 779-786.

12. Wittmann, A. and Suess, B. (2011) Selection of tetracycline inducible self-cleaving ribozymes as synthetic devices for gene regulation in yeast. *Mol Biosyst*, **7**, 2419-2427.

13. Chen, X., Denison, L., Levy, M. and Ellington, A.D. (2009) Direct selection for ribozyme cleavage activity in cells. *RNA*, **15**, 2035-2045.

14. Lynch, S.A. and Gallivan, J.P. (2009) A flow cytometry-based screen for synthetic riboswitches. *Nucleic Acids Res*, **37**, 184-192.

15. Fowler, C.C., Brown, E.D. and Li, Y. (2008) A FACS-based approach to engineering artificial riboswitches. *Chembiochem*, **9**, 1906-1911.

16. Desai, S.K. and Gallivan, J.P. (2004) Genetic screens and selections for small molecules based on a synthetic riboswitch that activates protein translation. *J Am Chem Soc*, **126**, 13247-13254.

17. Topp, S. and Gallivan, J.P. (2008) Random walks to synthetic riboswitches--a high-throughput selection based on cell motility. *Chembiochem*, **9**, 210-213.

18. Nomura, Y. and Yokobayashi, Y. (2007) Dual selection of a genetic switch by a single selection marker. *Biosystems*, **90**, 115-120.

19. Elowitz, M.B., Levine, A.J., Siggia, E.D. and Swain, P.S. (2002) Stochastic gene expression in a single cell. *Science*, **297**, 1183-1186.

20. Raser, J.M. and O'Shea, E.K. (2004) Control of stochasticity in eukaryotic gene expression. *Science*, **304**, 1811-1814.

21. Khvorova, A., Lescoute, A., Westhof, E. and Jayasena, S.D. (2003) Sequence elements outside the hammerhead ribozyme catalytic core enable intracellular activity. *Nat Struct Biol*, **10**, 708-712.

22. London, R.E. (1991) Methods for measurement of intracellular magnesium: NMR and fluorescence. *Annu Rev Physiol*, **53**, 241-258.

23. Canny, M.D., Jucker, F.M., Kellogg, E., Khvorova, A., Jayasena, S.D. and Pardi, A. (2004) Fast cleavage kinetics of a natural hammerhead ribozyme. *J Am Chem Soc*, **126**, 10848-10849.

24. Koch, A.L. and Lamont, W.A. (1956) The metabolism of methylpurines by Escherichia coli. II. Enzymatic studies. *J Biol Chem*, **219**, 189-201.

25. Win, M.N. and Smolke, C.D. (2008) Higher-order cellular information processing with synthetic RNA devices. *Science*, **322**, 456-460.

26. Andersson, J., Simpson, D.M., Qi, M., Wang, Y. and Elion, E.A. (2004) Differential input by Ste5 scaffold and Msg5 phosphatase route a MAPK cascade to multiple outcomes. *EMBO J*, **23**, 2564-2576.

27. Dufour, D., de la Pena, M., Gago, S., Flores, R. and Gallego, J. (2009) Structure-function analysis of the ribozymes of chrysanthemum chlorotic mottle viroid: a loop-loop interaction motif conserved in most natural hammerheads. *Nucleic Acids Res*, **37**, 368-381.

28. Perreault, J., Weinberg, Z., Roth, A., Popescu, O., Chartrand, P., Ferbeyre, G. and Breaker, R.R. (2011) Identification of hammerhead ribozymes in all domains of life reveals novel structural variations. *PLoS Comput Biol*, **7**, e1002031.

29. Seehafer, C., Kalweit, A., Steger, G., Graf, S. and Hammann, C. (2011) From alpaca to zebrafish: hammerhead ribozymes wherever you look. *RNA*, **17**, 21-26.

30. Alper, H., Fischer, C., Nevoigt, E. and Stephanopoulos, G. (2005) Tuning genetic control through promoter engineering. *Proc Natl Acad Sci U S A*, **102**, 12678-12683.

31. Nevoigt, E., Kohnke, J., Fischer, C.R., Alper, H., Stahl, U. and Stephanopoulos, G. (2006) Engineering of promoter replacement cassettes for fine-tuning of gene expression in Saccharomyces cerevisiae. *Appl Environ Microbiol*, **72**, 5266-5273.

32. Babiskin, A.H. and Smolke, C.D. (2011) A synthetic library of RNA control modules for predictable tuning of gene expression in yeast. *Mol Syst Biol*, **7**, 471.

33. Sambrook J, R.D. (2001) *Molecular Cloning: A Laboratory Manual, 3rd edn*. Cold Spring Harbor Lab Press, Cold Spring Harbor, NY.

34. Uppaluri, R. and Towle, H.C. (1995) Genetic dissection of thyroid hormone receptor beta: identification of mutations that separate hormone binding and transcriptional activation. *Mol Cell Biol*, **15**, 1499-1512.

35. Shaner, N.C., Campbell, R.E., Steinbach, P.A., Giepmans, B.N., Palmer, A.E. and Tsien, R.Y. (2004) Improved monomeric red, orange and yellow fluorescent proteins derived from Discosoma sp. red fluorescent protein. *Nat Biotechnol*, **22**, 1567-1572.

36. Gari, E., Piedrafita, L., Aldea, M. and Herrero, E. (1997) A set of vectors with a tetracycline-regulatable promoter system for modulated gene expression in Saccharomyces cerevisiae. *Yeast*, **13**, 837-848.

37. Sikorski, R.S. and Hieter, P. (1989) A system of shuttle vectors and yeast host strains designed for efficient manipulation of DNA in Saccharomyces cerevisiae. *Genetics*, **122**, 19-27.

38. Gietz, R.D. and Woods, R.A. (2002) Transformation of yeast by lithium acetate/single-stranded carrier DNA/polyethylene glycol method. *Methods Enzymol*, **350**, 87-96.

39. Siekhaus, D.E. and Drubin, D.G. (2003) Spontaneous receptor-independent heterotrimeric G-protein signalling in an RGS mutant. *Nat Cell Biol*, **5**, 231-235.

40. Guldener, U., Heck, S., Fielder, T., Beinhauer, J. and Hegemann, J.H. (1996) A new efficient gene disruption cassette for repeated use in budding yeast. *Nucleic Acids Res*, **24**, 2519-2524.

41. Flotho, A., Simpson, D.M., Qi, M. and Elion, E.A. (2004) Localized feedback phosphorylation of Ste5p scaffold by associated MAPK cascade. *J Biol Chem*, **279**, 47391-47401.

42. Chao, G., Lau, W.L., Hackel, B.J., Sazinsky, S.L., Lippow, S.M. and Wittrup, K.D. (2006) Isolating and engineering human antibodies using yeast surface display. *Nat Protoc*, **1**, 755-768.

43. Sprague, G.F., Jr. (1991) Assay of yeast mating reaction. *Methods Enzymol*, **194**, 77-93.

44. Hertel, K.J., Pardi, A., Uhlenbeck, O.C., Koizumi, M., Ohtsuka, E., Uesugi, S., Cedergren, R., Eckstein, F., Gerlach, W.L., Hodgson, R. *et al.* (1992) Numbering system for the hammerhead. *Nucleic Acids Res*, **20**, 3252.

45. Mathews, D.H., Disney, M.D., Childs, J.L., Schroeder, S.J., Zuker, M. and Turner, D.H. (2004) Incorporating chemical modification constraints into a dynamic programming algorithm for prediction of RNA secondary structure. *Proc Natl Acad Sci U S A*, **101**, 7287-7292.

46. Darty, K., Denise, A. and Ponty, Y. (2009) VARNA: Interactive drawing and editing of the RNA secondary structure. *Bioinformatics*, **25**, 1974-1975.